AD_____

Award Number: W81XWH-11-1-0248

TITLE: Echo-Planar Imaging Based J-Resolved Spectroscopic Imaging for Improved
Metabolite Detection in Prostate Cancer

PRINCIPAL INVESTIGATOR: Michael Albert Thomas Ph.D.

CONTRACTING ORGANIZATION:

University of California, Los Angeles
Los Angeles, CA 90024-1406

REPORT DATE: October 2013

TYPE OF REPORT: Annual

PREPARED FOR: U.S. Army Medical Research and Materiel Command
Fort Detrick, Maryland 21702-5012

DISTRIBUTION STATEMENT: Approved for Public Release;
Distribution Unlimited

The views, opinions and/or findings contained in this report are those of the author(s) and
should not be construed as an official Department of the Army position, policy or decision
unless so designated by other documentation.

REPORT DOCUMENTATION PAGE

Public reporting burden for this collection of information is estimated to average 1 hour per response, including the time for reviewing instructions, searching existing data sources, gathering and maintaining the data needed, and completing and reviewing this collection of information. Send comments regarding this burden estimate or any other aspect of this collection of information, including suggestions for reducing this burden to Department of Defense, Washington Headquarters Services, Directorate for Information Operations and Reports (0704-0188), 1215 Jefferson Davis Highway, Suite 1204, Arlington, VA 22202-4302. Respondents should be aware that notwithstanding any other provision of law, no person shall be subject to any penalty for failing to comply with a collection of information if it does not display a currently valid OMB control number. **PLEASE DO NOT RETURN YOUR FORM TO THE ABOVE ADDRESS.**

1. REPORT DATE	2. REPORT TYPE	3. DATES COVERED
October 2013	Annual	30September2012– 29September2013

4. TITLE AND SUBTITLE

Echo-Planar Imaging Based J-Resolved Spectroscopic Imaging for Improved Metabolite Detection in Prostate Cancer

5a. CONTRACT NUMBER
W81XWH-11-1-0248

5b. GRANT NUMBER
W81XWH-11-1-0248

5c. PROGRAM ELEMENT NUMBER

6. AUTHOR(S)
Michael Albert Thomas Ph.D.

E-Mail: athomas@mednet.ucla.edu

5d. PROJECT NUMBER

5e. TASK NUMBER

5f. WORK UNIT NUMBER

7. PERFORMING ORGANIZATION NAME(S) AND ADDRESS(ES) AND ADDRESS(ES)

University of California, Los Angeles
 Los Angeles, CA 90095

8. PERFORMING ORGANIZATION REPORT NUMBER

9. SPONSORING / MONITORING AGENCY NAME(S) AND ADDRESS(ES)
U.S. Army Medical Research and Materiel Command
Fort Detrick, Maryland 21702-5012

10. SPONSOR/MONITOR'S ACRONYM(S)

11. SPONSOR/MONITOR'S REPORT NUMBER(S)

12. DISTRIBUTION / AVAILABILITY STATEMENT
Approved for Public Release; Distribution Unlimited

13. SUPPLEMENTARY NOTES

14. ABSTRACT

Purpose: 1) To implement an echo-planar imaging (EPI)-based 2D J-resolved spectroscopy on a 3T MRI/MRS scanner;2) To evaluate the multi-voxel 2D J-resolved echo-planar spectroscopic imaging (EP-JRESI) in malignant PCa patients, benign prostatic hyperplasia (BPH) patients and healthy prostates. 3) To develop and further optimize the ProFit algorithm to post-process the multi-dimensional MRS data from different prostate pathologies.
Scope: A major outcome is expected to be on improved detection (specificity) in differentiating malignant from benign prostate cancer using a novel four-dimensional (4D) EP-JRESI. Improved spectroscopic imaging techniques will enable unambiguous detection of metabolites and the lipids in situ, which could potentially complement the existing diagnostic modalities commonly used in prostate cancer.
Progress and Major Findings: After the successful implementation of the 4D EP-JRESI sequence on a 3T MRI scanner during the 1st year, multi-voxel 2D J-resolved spectra have been recorded in 7 more male subjects (6 patients and 1 healthy) using endorectal as well as external MRI coils. The findings are reproducible with that obtained in the 1st year and the EP-JRESI data had excellent quality. Two peer-reviewed manuscripts have been published during the second year.

15. SUBJECT TERMS: Digital Rectal Examination, prostate specific antigen, Four Dimensional (4D) Echo-Planar J-Resolved Spectroscopic Imaging (EP-JRESI); Citrate, Choline, Creatine, Spermine, 3Tesla MRI scanner, Endo-rectal MR coil, WET Water Suppression, prostate cancer (PCa), benign prostatic hyperplasia (BPH), prior-knowledge fitting

16. SECURITY CLASSIFICATION OF:			17. LIMITATION OF ABSTRACT	18. NUMBER OF PAGES	19a. NAME OF RESPONSIBLE PERSON USAMRMC
a. REPORT	**b. ABSTRACT**	**c. THIS PAGE**			
U	U	U	UU	31	**19b. TELEPHONE NUMBER** *(include area code)*

Table of Contents

Introduction: Prostate cancer (PCa) is the most common cancer in men in several countries, with the American Cancer Society (ACS) estimating 241,740 new cases of PCa to be diagnosed and deaths of 28,170 men of PCa (1). Due to its prevalence in the male population as well as its unpredictable clinical course, early detection and diagnosis have become a priority for many health care professionals. Another method for staging prostate cancer is through imaging techniques including ultrasound, computed tomography (CT), and magnetic resonance imaging (MRI) with or without the help of dynamic contrast enhancement modeling (DCE-MRI), diffusion weighted imaging (DWI), and magnetic resonance spectroscopy (MRS) (2-5). MRS is a powerful tool for exploring the cellular chemistry of human tissues (3,5,6-11). There is a growing body of evidence that 1H MRS may contribute to the clinical evaluation of prostate cancer and also for evaluating the metabolic alterations due to therapy. There have been no reports on combining two spectral dimensions with two-dimensional (2D) or three dimensional (3D) spatial encoding applicable to prostate cancer. Acceleration of magnetic resonance spectroscopic imaging (MRSI) has been demonstrated using echo-planar imaging techniques (12-13). Recently, Schulte et al. have successfully developed an algorithm called prior-knowledge fitting (ProFit) to quantify metabolite concentrations using the JPRESS spectra recorded using a Philips 3T MRI scanner (14). It was demonstrated that metabolite quantitation of JPRESS spectra with ProFit was accurate, robust and yielding generally consistent results, both *in vivo* and *in vitro*. Their results suggest that the number of quantifiable prostate metabolites can be increased from 3-4 with 1D PRESS/LC-Model to more than 10 with JPRESS/ProFit (15-16).

Body:
*i) **Proposed Task 1** (**Months 1-6**): To implement a multi-voxel based extension of the JPRESS sequence, in which two spectral encodings will be combined with two spatial encodings using the new Siemens VB17a platform. This four-dimensional (4D) data acquisition scheme will be accomplished utilizing the EPI approach that is commonly used for spatial encoding in MRI.*

Completed and Reported in the 1st year Annual Report.

*ii) **Proposed Task 2:** To evaluate the EPI-based JPRESS using a prostate phantom containing several metabolites which have been reported in prostate tissues, and to optimize the EP-JJRESI sequence and other acquisition parameters using the phantom (**Months 6-12**).*

Completed and Reported in the 1st year Annual Report.

*iv) **Proposed Task 3:** To record the 4D EP-JRESI spectra in the peripheral, central and transition zones of healthy prostates. (**Months 6-18**).*

Completed partially and Reported in the 1st year Annual Report. More work is in progress.
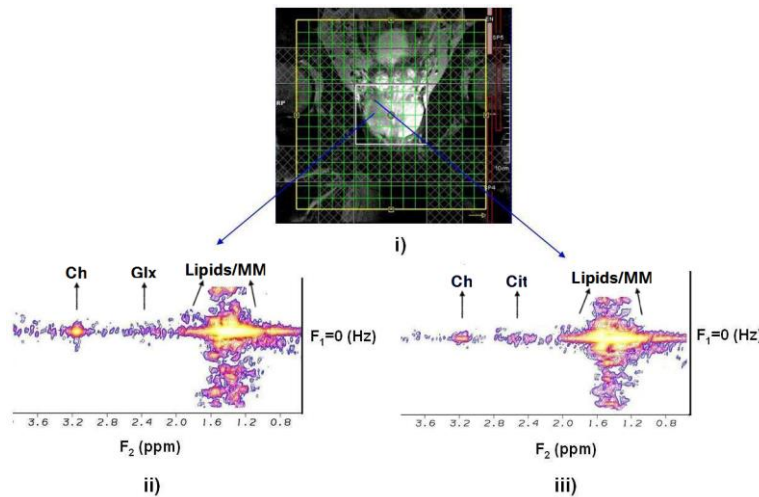
***Proposed Task 4:** To develop, evaluate and optimize the prior-knowledge basis set spectra using the GAMMA-simulation and prostate phantom solutions as prior*

knowledge for the multi-voxel based JPRESS spectra recorded using the 3T MRI scanner (Months 6-12).

Accomplished during September 29, 2011-October 28 2012:

***Proposed Task* 5:** To record the multi-voxel-based 2D spectra in the peripheral, central and transition zones of patients with BPH and malignant prostate cancer. The prostate metabolite concentrations calculated using the ProFit algorithm prepared for the multi-voxel data will be compared with LC-Model processed 1D spectral based MRSI data (**Months 18-36**).

Accomplished during October 29, 2012-October 28 2013: We present our recent results from 2 malignant prostate cancer patients. The following parameters were used to acquire the 4D EP-JRESI data: TR/TE=1.5s/30ms, 2 averages, 512 t_2, oversampled $32k_x$, 64 increments along the indirect spectral (t_1) and 16 spatial k_y dimensions; the endorectal "receive" coil. First, the 4D NUS EP-JRESI data was acquired in a 61 year old PCa patient having PSA of 9.1 and two malignant lesions (GS3+4 in the right base and GS4+3 in the right mid regions) and extracted spectra from 2 different locations (1ml)

Figure 1. i) a coronal T_2W *slice showing the multi-voxel EP-JRESI grids; extracted 2D JPRESS spectra of malignant voxels (1ml) from the right mid (ii) and right base (iii)* **portions**

after the CS reconstruction are shown in Figure 1. The top insert (i) shows the multi-voxel grid overlaid on an T_2W coronal slice; the extracted two spectra from the malignant masses in the right mid (GS4+3) (ii) and right base (iii) regions.

Shown in the extracted tumor spectra of this 61 year old patient with two different lesions (GS3+4 and GS 4+3) are the following: significantly increased Ch and significantly decreased Cit, Spm, mI, Tau and sI demonstrating more metabolite changes than the commonly reported few metabolite changes using the conventional 3D MRSI technique with average weighted encoding. It is also seen that the lesion with GS4+3 shows more significant changes of above mentioned metabolites, and also, elevated Glx (Glu+Gln) in agreement with a recent HR-MAS analysis of radically resected prostate specimens by Gribbestad and co-workers (17). Presence of an additional peak in GS4+3 at 2.8ppm was indicative of the elevated ω6 fatty acids as reported recently (18)

Second, shown in Fig.2 is the 4D NUS EP-JRESI data acquired in a 72 year old PCa patient having PSA of 5.6 and GS 4+3 and extracted spectra from a cancer location location (1ml).
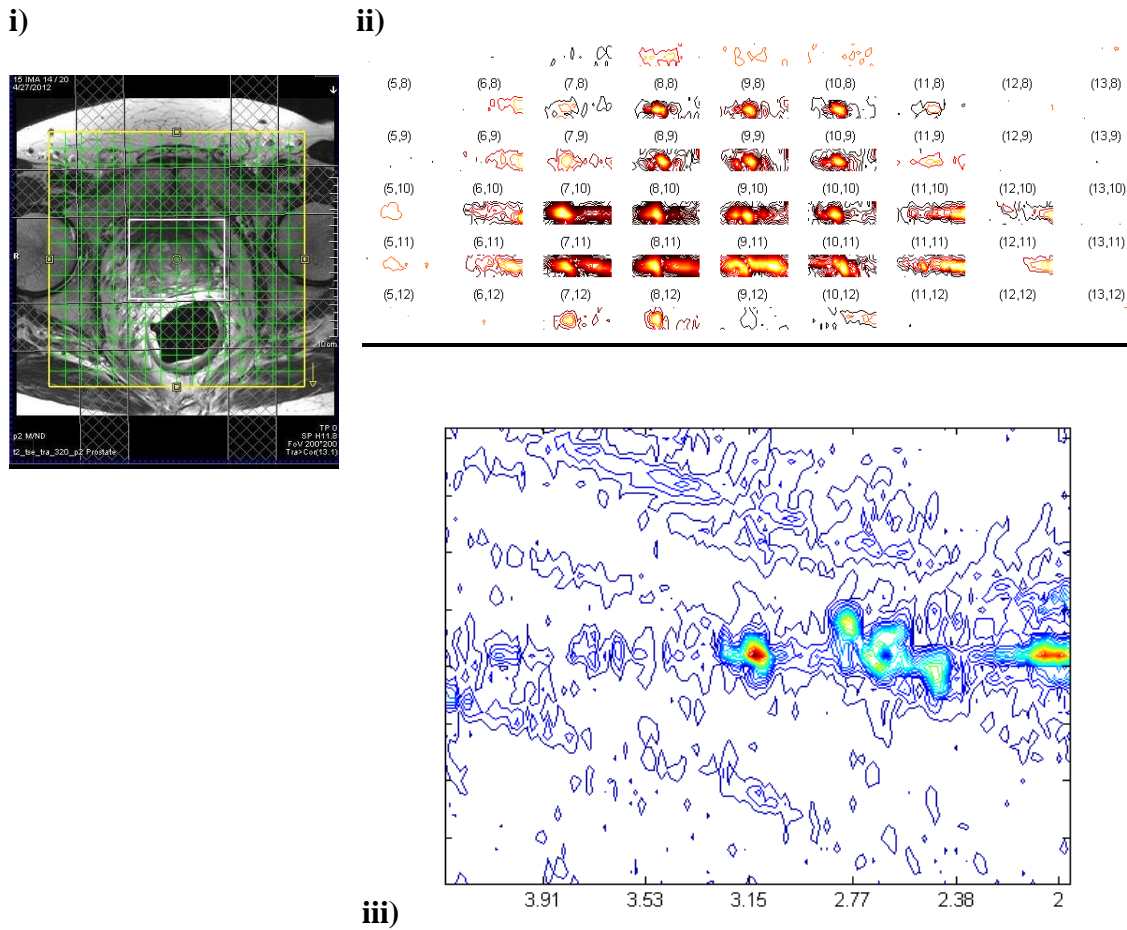
i)

ii)

iii)

Figure 2. *i) An axial* T$_2$W *MRI slice showing the multi-voxel EP-JRESI grids; ii) multi-voxel display of Ch and Cr peaks and an extracted 2D JPRESS spectrum from one of malignant voxels (iii).*

Key Research Accomplishments

- Continued evaluation of the 4D EP-JRESI sequence in 6 malignant prostate cancer patients and one healthy male subject.
- We have made further progress on compressed sensing reconstruction of the non-uniformly undersampled 4D EP-JRESI sequence using different reconstruction methods such as maximum entropy, total variation (TV), etc . This will facilitate shortening the endorectal spectral acquisition and reducing the patient inconvenience during the scan.
- Using the preliminary results obtained using this IDEA grant, we had reported our failed attempt on an R01 application entitled "EchoPlanar J-resolved Prostate Cancer Metabolite Imaging Using Compressed Sensing" that was submitted to the National Institute of health (NIH) in July2012/October 2011 (32nd percentile). Hence, a new NIH R01 grant application entitled "Fast J-resolved Prostate MR Spectroscopic Imaging and Non-linear Reconstruction" was submitted on October 5, 2013 using the preliminary results from this IDEA grant.

6

Reportable Outcomes:

A. Peer-reviewed Publications:
1. Nagarajan R, Margolis D, Raman S, et al. MR Spectroscopic Imaging of Peripheral zone in Prostate Cancer using a 3T MRI scanner: Endorectal versus External Phased array Coils. Magnetic Resonance Insights 2013: 6: 51-58 [**PMID: N/A**].
2. Thomas MA, Nagarajan R, Huda A, et al. Multidimensional MR Spectroscopic imaging of Prostate Cancer In vivo. NMR in Biomed 2013 July 31(Epub ahead of print). [**PMID: 23904127**].

B. Presentations: During the 2nd year, the first abstract entitled "Accelerated Four-Dimensional Echo-Planar J-Resolved Spectroscopic Imaging of Human Prostate: Prospective Non-Uniform Undersampling and Maximum Entropy Reconstruction." was submitted and presented at the 54th Experimental Nuclear Magnetic Resonance (ENC), Asilomar, CA, Abstract #214, (April 14-19, 2013). The 2nd abstract entitled "Nonuniformly Under-Sampled (NUS) Echo Planar J-Resolved Spectroscopic Imaging (EP-JRESI) of Prostate Cancer Patients and Compressed Sensing Reconstruction" summarizing the implementation of the 4D EP-JRESI sequence and evaluation of it in the prostate cancer patients was presented at the 21st International Society of Magnetic Resonance in Medicine (ISMRM), Salt Lake, Utah, April 20-26, 2013, #3959.

C. Books: None on Prostate Cancer Research based.

Conclusions: After successfully implementing the 4D EP-JRESI scanning protocol on the 3T MRI scanner and testing it in healthy controls and patients during the 1st year, 7 more subjects have been scanned in this year. We will continue to recruit 20 malignant and 5 benign prostate cancer patients, and 5 healthy male subjects during the next year.

References

1) Dall'era MA, Cooperberg MR, Chan JM, *et al*. Active surveillance for early-stage prostate cancer: review. Cancer. 2008 Apr 15;112(8):1650-9. **PMID: 18306379**
2) McNeal JE. Normal histology of the prostate. Am J Surg Pathol 1988;12:619-633. **PMID: 2456702**
3) Weinreb JC, Blume JD, Coakley FV, et al. Prostate cancer: sextant localization at MR imaging and MR spectroscopic imaging before prostatectomy--results of ACRIN prospective multi-institutional clinicopathologic study. Radiology. 2009 Apr;251(1):122-33. **PMID: 19332850**
4) Jacobs MA, Ouwerkerk R, Petrowski K and Macura KJ. Diffusion-weighted imaging with apparent diffusion coefficient mapping and spectroscopy in prostate cancer. Top Magn Reson Imaging. 2008;19:261-72 **PMID:19512848**
5) Scheenen TW, Heijmink SW, Roell SA, et al. Three-dimensional proton MR Spectroscopy of human prostate at 3T without endorectal coil: feasibility. Radiology 2007;245:507-16. **PMID: 17848681**
6) Thomas MA, Narayan P, Kurhanewicz J, Jajodia P, Weiner MW. 1H MR spectroscopy of normal and malignant human prostates in vivo. J Magn Reson 1990; 87:610–619. **PMID:N/A**

7) Thomas MA, Narayan P, Kurhanewicz J, *et al*. Detection of phosphorus metabolites in human prostates with a transrectal ^{31}P NMR probe. J Magn Reson 1992; 99: 377-386. **PMID: N/A**

8) Narayan P, Kurhanewicz J. Magnetic Resonance spectroscopy in prostate disease: diagnostic possibilities and future developments. Prostate 1992; Suppl 4: 43-50. **PMID: 1374177**

9) van der Graaf M, Schipper RG, Oosterhof GO, J.A. Schalken, AA. Proton MR spectroscopy of prostatic tissue focused on the detection of spermine, a possible biomarker of malignant behavior in prostate cancer. MAGMA 2000; 10(3):153-9. **PMID: 10873205**

10) Jordan KW and Cheng LL. NMR-based metabolomics approach to target biomarkers for human prostate cancer. Expert Rev Proteomics 2007;4:389-400. **PMID: 17552923**

11) Kurhanewicz J, Swanson MG, Nelson SJ, and Vigneron DB. Combined magnetic resonance imaging and spectroscopic imaging approach to molecular imaging of prostate cancer. J Magn Reson Imaging 2002;16(4):451-463. **PMID: 12353259**

12) Mansfield P. Spatial mapping of the chemical shift in NMR. Magn Reson Med 1984; 1: 370 – 386. PMID:6571566

13) Posse S, Otazo R, Caprihan A, et al. Proton echo-planar spectroscopic imaging of J-coupled resonances in human brain at 3 and 4 Tesla. Magn Reson Med 2007; 58(2): 236-44. PMID: 17610279

14) Schulte RF and Boesiger P. ProFit: two-dimensional prior-knowledge fitting of J-resolved spectra. NMR Biomed 2006;19:255-263. **PMID: 16541464**

15) Lange T, Schulte RF and Boesiger P. Quantitative J-resolved prostate spectroscopy using two-dimensional prior-knowledge fitting. Magn Reson Med 2008;59:966-972. PMID: 18429013

16) Thomas MA, Lange T, Velan SS, et al. Two-dimensional MR Spectroscopy of healthy and cancerous prostates in vivo. Magn Reson Mater Phy (MAGMA) 2008;21(6):443-58. **PMID**: **18633659**

17) Wright A, Tessem MB, Bertilsson H, et al. Quantitative 1H HR-MAS using LC Model shows glutamate, choline, glycerylphosphocholine, and glucose as biomarkers of prostate. Proc Intl Soc Magn Reson Med 2012;20:2975. **PMID: N/A**

18) Stenman K, Hauksson JB, Grobner G, et al. Detection of polyunsaturated omega-6 fatty acid in human malignant prostate tissue by 1D and 2D high resolution magic angle spinning NMR spectroscopy. MAGMA 2009;22:327-31 **PMID: 19921294.**

Appendix:

1. Nagarajan R, Margolis D, Raman S, et al. MR Spectroscopic Imaging of Peripheral zone in Prostate Cancer using a 3T MRI scanner: Endorectal versus External Phased array Coils. Magnetic Resonance Insights 2013: 6: 51-58.

2. Thomas MA, Nagarajan R, Huda A, et al. Multidimensional MR Spectroscopic imaging of Prostate Cancer In vivo. NMR in Biomed 2013 July 31(Epub ahead of print).

ORIGINAL RESEARCH

MR Spectroscopic Imaging of Peripheral Zone in Prostate Cancer Using a 3T MRI Scanner: Endorectal versus External Phased Array Coils

Rajakumar Nagarajan[1], Daniel JA Margolis[1], Steven S. Raman[1], David Ouellette[1], Manoj K. Sarma[1], Robert E. Reiter[2] and M. Albert Thomas[1]

[1]Radiological Sciences, University of California Los Angeles, Los Angeles, CA, USA. [2]Urology, University of California Los Angeles, Los Angeles, CA, USA. Corresponding author email: athomas@mednet.ucla.edu

Abstract: Magnetic resonance spectroscopic imaging (MRSI) detects alterations in major prostate metabolites, such as citrate (Cit), creatine (Cr), and choline (Ch). We evaluated the sensitivity and accuracy of three-dimensional MRSI of prostate using an endorectal compared to an external phased array "receive" coil on a 3T MRI scanner. Eighteen patients with prostate cancer (PCa) who underwent endorectal MR imaging and proton (1H) MRSI were included in this study. Immediately after the endorectal MRSI scan, the PCa patients were scanned with the external phased array coil. The endorectal coil-detected metabolite ratio [(Ch+Cr)/Cit] was significantly higher in cancer locations (1.667 ± 0.663) compared to non-cancer locations (0.978 ± 0.420) ($P < 0.001$). Similarly, for the external phased array, the ratio was significantly higher in cancer locations (1.070 ± 0.525) compared to non-cancer locations (0.521 ± 0.310) ($P < 0.001$). The sensitivity and accuracy of cancer detection were 81% and 78% using the endorectal 'receive' coil, and 69% and 75%, respectively using the external phased array 'receive' coil.

Keywords: prostate cancer, MRSI, metabolites, external coil, sensitivity, citrate, choline, creatine

This article is available from http://www.la-press.com.

Introduction

Prostate cancer (PCa) is the most common non-cutaneous cancer and second leading cause of cancer death in men. In 2012, approximately 241,740 new cases and 28,170 PCa-related deaths occurred in the United States.[1] Magnetic resonance imaging (MRI) has been used to evaluate prostate anatomy and prostate pathologies for several years. MRI, with its excellent soft-tissue differentiation, provides high-resolution images of the prostate and surrounding structures. Magnetic resonance spectroscopy (MRS) is a powerful tool for exploring the cellular chemistry of human tissues.[2–6] There is a growing body of evidence that proton MRS can be used for clinical evaluation of PCa and metabolic alterations before and after therapy. Magnetic resonance spectroscopic imaging (MRSI) can be used to measure metabolite levels in the tissue, particularly choline (Ch), citrate (Cit), creatine (Cr), and various polyamines (spermine, spermidine, and putrecine). PCa typically shows an increased concentration of Ch and reduction of Cit and polyamines.

MRSI of the prostate is typically performed using a combination of point-resolved spectroscopy (PRESS)[7] and three-dimensional localized MRSI[8] rather than the traditional single-voxel or slice-based two-dimensional MRSI technique was used in brain spectroscopic imaging. 3D MRSI requires phase encoding along the three spatial dimensions, conventionally known as frequency, phase, and slice. Acquisition time and coverage of the prostate are the primary considerations in choosing matrix dimensions. Acquiring 3D MRSI data with higher spatial resolution requires a long total acquisition time. Conventional prostate MRSI studies involving average weighted encoding use a long echo time (TE) with a short repetition time (TR), allowing observation of a reduced number of metabolites.[9] Long TEs are used for 3D MRSI due to the addition of MEGA[10] radio-frequency pulses for both water and lipid suppression. The interpretation system most used to discriminate between cancer and normal prostatic tissue in the peripheral zone was described by Kurhanewicz et al.[9] They calculated the peak area ratios of Ch and Cr to Cit [(Ch+Cr)/Cit] for each voxel. Inclusion of Cr in this ratio is mandatory because of the Cr peak is very close to the Ch peak in the spectrum. However, Cr appears be maintained at a relatively constant level in both healthy and tumor prostatic tissues.

It was unknown whether the quality of endorectal MRSI scanning could be improved by using a stronger (3T) scanner and/or using perfluorocarbon (PFC) in the endorectal coil (ERC) instead of air. Rather than filling air, PFC has been shown to improve MRSI image quality and the magnetic susceptibility closely matching that of prostate.[11] The ERC is contraindicated in a number of patients (eg, after abdominal perineal resection for rectal cancers or after radiation therapy for the pelvis).[12] In some cases, it is preferable to not use an ERC to avoid structural deformation of the prostate peripheral zone, which is often compressed by an ERC. The ERC also causes signal hyperintensity near the rectum and the neighboring peripheral zone. Signal hyperintensity and tissue deformation can make complicate diagnostic interpretation. Previous studies have reported the use of external phased array coils for prostate MR spectroscopy in 3T.[13–20] The major goal of the study was to evaluate 3T MRSI for the peripheral zone in prostate cancer patients using an endorectal coil and to compare the performance of 3T MRSI and an external phased array 'receive' coil.

Materials and Methods

Eighteen patients ranging in age from 56–72 years (mean, 63.1 years) with PCa who underwent endorectal MR imaging and proton MR spectroscopic imaging were included in this study. The study protocol was approved by the Institutional Review Board, and informed consent was obtained from each patient. Gleason scores for the tumor on prostate biopsy ranged from 3 to 8, while prostate-specific antigen varied from 2.8 to 20.6 ng/mL (mean of 6.84 ng/mL). A Siemens 3T MRI Scanner with high-performance gradients (Trio-Tim, Siemens Medical Solutions, Erlangen, Germany) was used in this investigation. A quadrature body 'transmit' coil was used to transmit radio-frequency pulses. An endorectal inflatable 'receive' coil (Medrad Corporation, Indianola, PA, USA) was then inserted into the rectum and inflated with 50 cc PFC. The coil was positioned horizontally at approximately the 10:00 and 2:00 positions. After endorectal scanning, patients were scanned with the external phased array 'receive' coil for the comparison study. T_2-weighted images in the transverse, sagittal, and coronal planes were acquired by using a turbo spin-echo sequence. The MRI protocol included

T_2-weighted images acquired using a fast spin-echo sequence with: repetition time (TR) = 3,800 ms, effective echo time (TE) = 101 ms, slice thickness = 3 mm, field of view = 140 mm, and matrix size = 256×256 mm^2. MRSI was performed in all patients, which included a 3D water- and fat-suppressed spectroscopic acquisition. 3D MRSI parameters of the endorectal and external phased array coil were as follows: TR 750 ms, TE 145 ms, acquisition bandwidth 1250 Hz, 6 averages, and 512 spectral data points with a voxel resolution of 0.3 mL. Total acquisition time was approximately 12 min. For the external phased array, the voxel resolution was 0.35 mL. A PRESS-based sequence was used to acquire proton MR spectra from a volume of interest (VOI) of approximately $55 \times 45 \times 45$ mm^3. Outer volume suppression of water and lipid was achieved using eight 3-cm thick saturation pulses around the VOI.

A spectroscopist examined the MRSI data set and reported the location and number of suspicious voxels to the radiologist, to identify metabolite ratios predictive of cancer. For 3D MRSI post-processing, each spectrum was Fourier transformed, frequency-, phase-, and baseline-corrected, and the peaks of Cit, Ch, and Cr were subsequently fitted. A Hamming filter was used for the MRSI spatial dimensions of the data. For tumor localization, the prostate was split along the midline and further divided into the apex, the middle, and the base of the gland. According to histopathologic findings, the voxels and corresponding spectra were assigned as normal tissue or tumor tissue. For selected voxels in the peripheral zone, the area under the curve of the metabolite resonances was determined and the signal intensity ratio for (Ch+Cr)/Cit was calculated using commercially available software from Siemens. Peak areas for Ch, Cr, Spm, and Cit were calculated using numeric integration. Metabolic maps of (Ch+Cr)/Cit were generated since Spm cannot be separated from Ch and Cr peaks. Voxels were considered suitable if they consisted of at least 75% peripheral zone tissue and did not include periurethral tissue. If the Cit peak was lower than the Ch peak or was undetectable, the voxel was determined to be malignant. If the Cit peak was higher than the Ch peak, the voxel was considered noncancerous for (Ch+Cr)/Cit values smaller than 0.50 and malignant for (Ch+Cr)/Cit values greater than 0.50.

For the external phased array coil, the noncancerous ratio was less than 0.28 and the malignant ratio was greater than 0.28.

The paired t-test was used to determine whether the ratios of (Ch+Cr)/Cit in cancer were different from those in non-cancer using an endorectal coil and external coil. A P-value less than 0.05 was considered statistically significant.

Receiver operating characteristic (ROC) curve analyses based on logistic regression models were performed to identify the optimal cutoff value for predicting metabolite ratios using the endorectal coil and external phased array coil. The area under the curve (AUC), interpreted as the average value of sensitivity for all possible values of specificity, was used in the ROC analysis. An area of 0.50 implies that the variable adds no information, whereas an area of 1 implies perfect accuracy. Sensitivity, specificity, positive predictive value (PPV), and negative predictive value (NPV) as well as accuracy were reported for the optimal thresholds. P-values < 0.05 were considered statistically significant. Statistical analyses were performed using SPSS software (Statistical Package for the Social Sciences, Version 18.0, SPSS Inc, Chicago, IL, USA).

Results

Figure 1A and B show the metabolite ratios (Ch+Cr)/Cit for cancer and non-cancer locations with endorectal and external phased array coil in 18 PCa patients. For the endorectal coil, the metabolite ratio (mean ± SD) was significantly higher in cancer locations (1.667 ± 0.663) compared to in non-cancer locations (0.978 ± 0.420) ($P < 0.001$). Similarly, for the external phased array coil, the ratio was significantly higher in cancer locations (1.070 ± 0.525) than in non-cancer locations (0.521 ± 0.310) ($P < 0.001$). Figure 2A and B show a comparison of endorectal and external phased array MR Spectroscopic Imaging of a 67 year-old PCa patient. A significant elevation in Ch/Cr and decreased Cit were observed in the right side peripheral zone of the PCa patient scanned using endorectal coil. Similar trends for metabolite changes are shown in Figure 2B with a slightly worse signal-to-noise ratio (SNR) because the patient was scanned using an external coil. Table 1 shows the full width at half maximum (FWHM) of Cit and (Cr+Ch) in cancer and noncancerous locations using the
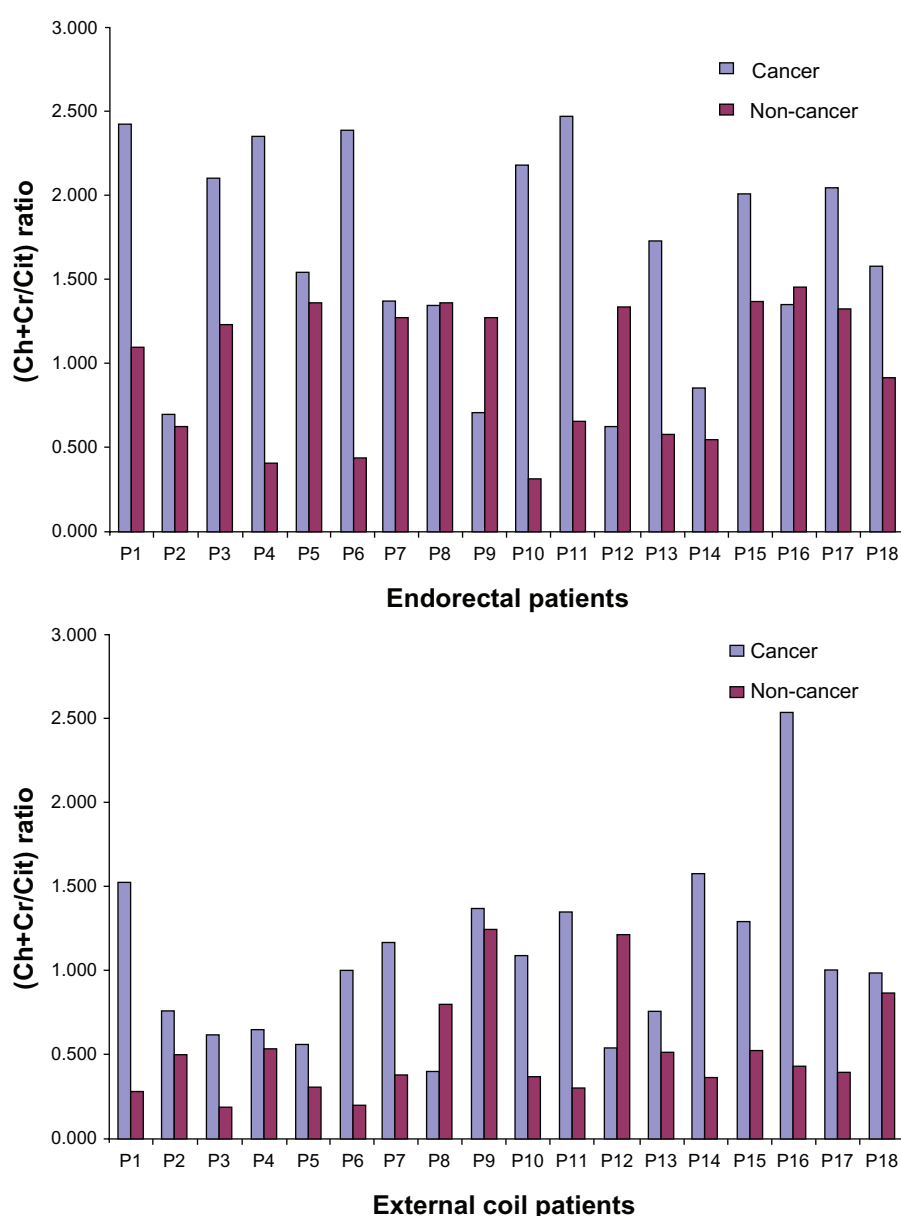
Figure 1. Comparison of metabolite ratios [(Ch+Cr)/Cit] in 18 PCa patients scanned with the endorectal and external body array 'receive' coils.
Note: Significant ($P < 0.05$) elevation of Ch/Cr observed in cancer locations compared to non-cancer locations in both coils.

endorectal and external phased array coil. The mean FWHM of Cit in cancer and non-cancer locations for patients scanned using the endorectal coil were 11.7 and 11.5 Hz respectively, whereas using the external coil, the mean FWHM values were 17.7 and 19.5 Hz, which showed a higher coefficient of variance (CV). Similarly, the mean FWHM of Ch+Cr in cancer and non-cancer locations of patients scanned using the endorectal coil were 17.7 and 19.5 Hz, where in the external coil, the mean FWHM values were 25.7 and 28 Hz with a higher CV. The mean global water line width of 25 Hz observed using the endorectal coil and

31 Hz was observed using the external phased array coil with higher CV.

Figure 3 shows that the MRSI metabolite ratios in peripheral zone cancer locations derived from endorectal coil- and external body coil were positively and linearly correlated ($R^2 = 0.571$). Figure 4 shows the comparison of receiver operating characteristics curves for the endorectal coil- and external body coil-derived MRSI ratio. ROC curve analyses for differentiating endorectal coil suggested an optimal cutoff value of 1.35. This implies that the proportions of correctly identified endorectal coil sensitivity, specificity,
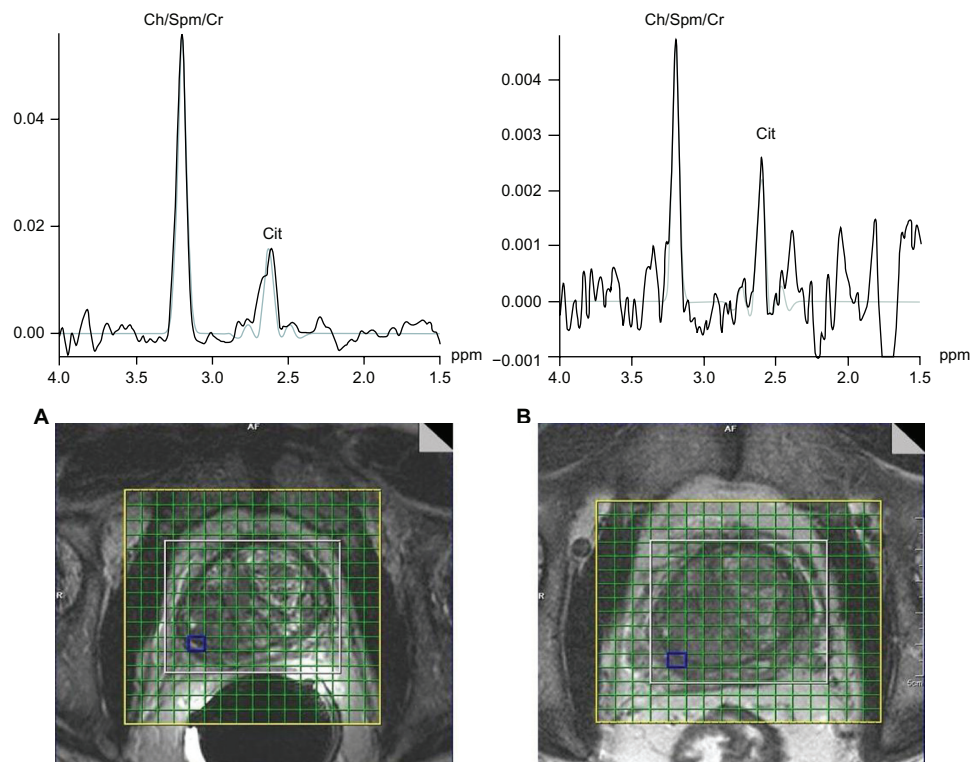
Figure 2. Comparison of (**A**) endorectal and (**B**) external body array MR Spectroscopic Imaging of a 67-year old PCa patient.
Note: Extracted single voxel spectra show a significant ($P < 0.05$) elevation of Ch/Cr and declined Cit in the right side peripheral zone of the PCa patient in both coils.

PPV, and NPV were 81.3%, 75.0%, 76.5%, and 80.0%, respectively. The AUC was 86.9%, with an accuracy of 78.1%. The cutoff value for the external body coil was 0.77 for sensitivity, specificity, and accuracy values of 68.8%, 81.3%, and 75.0%, respectively. The AUC of the MRSI ratio slightly increased for endorectal coil (86.9%) compared to external phased array coil (85.9%). In the evaluation of the endorectal coil versus external phased array coil, the MRSI ratios showed an accuracy of 78.1%, indicating good discrimination compared to external phased array of 75.0%. Detailed results of the ROC curve analyses

are shown in Table 2, which shows the sensitivity, specificity, PPV, NPV, AUC, and accuracy of classifying endorectal coil and external body coil.

Discussion

Numerous studies have suggested that MRSI using an ERC is the most promising technique for detecting and staging of PCa. At more commonly available clinical field strengths of 1.5T, an ERC is necessary for obtaining a sufficiently high SNR with subsequent spatial resolution, allowing reliable cancer delineation in a clinically reasonable time frame. However, the

Table 1. FWHM of water and metabolite resonances using endorectal and external body array "receive" coils.

Peak	Endorectal FWHM Mean ± SD	CV (%)	External body array FWHM Mean ± SD	CV (%)
Cancer Cit	11.73 ± 2.75	23.41	15.45 ± 6.17	39.96
Cancer (Cr+Ch)	17.71 ± 6.78	27.57	25.75 ± 8.47	32.88
Non-cancer Cit	11.53 ± 1.73	15.02	18.83 ± 10.16	53.94
Non-cancer (Cr+Ch)	19.59 ± 6.83	27.77	28.06 ± 10.80	38.49
Water	25.00 ± 5.16	20.64	31.00 ± 9.62	31.05

Note: The FWHM of the water resonance represents global line width whereas the FWHM values of metabolites were derived from spectra extracted from selected locations.
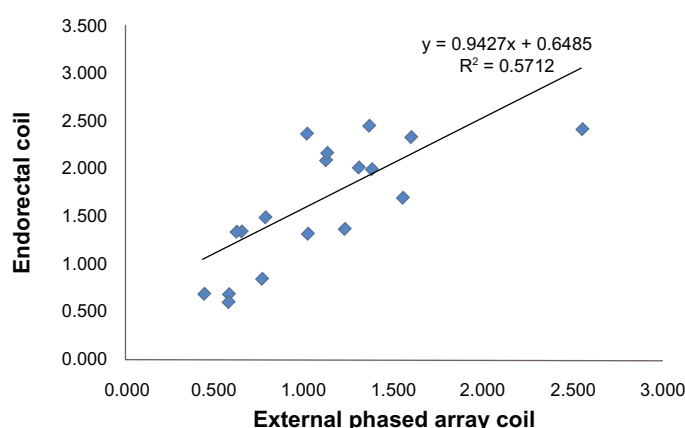
$$y = 0.9427x + 0.6485$$
$$R^2 = 0.5712$$

Figure 3. Correlation between the maximum ratios [(Ch+Cr)/Cit] of cancer identified in the peripheral zone with external phased array coil vs. endorectal coil MRS.
Note: A positive correlation was observed.

use of an ERC is more time-consuming, leading to higher costs and greater patient discomfort. Thus, we compared the performance of the endorectal coil with the external phased array coil at 3T.

Compared with external phased array coil at 3T, endorectal MR spectroscopy at 3T significantly improves spectral line width and coefficient of variance of metabolite ratio. The FWHM is a good indicator of spectral homogeneity. The FWHM value typically increases as VOI increases. Excellent quality of prostate spectra can be obtained through optimization of B_0 homogeneity for the PRESS-selected VOI. This procedure typically involves the combined use of a standard automatic shim provided by the manufacturer and, if necessary, manual adjustments of the linear x, y, and z gradients. Small improvements in shim can make a significant difference in spectra quality. Particularly, good B_0 homogeneity is essential

for sufficient water and lipid suppression. Water and lipid suppression is achieved through generation of frequency-selective MEGA pulses.[10] During MRSI acquisition, large lipid resonance peaks obscures the metabolite peak. Outer volume saturation pulses were used to eliminate signals from adjacent tissues, particularly periprostatic lipids and rectal wall tissue. The coefficient of variance was higher in the external phased array than for the endorectal coil due to the larger size of the coil and increased distance from the prostate proportional to abdominal circumference, leading to a decrease in the SNR ratio.

The overall accuracy of the external phased array coil MRSI has been shown to be slightly inferior to that using the endorectal coil in our pilot study involving a limited number of patients. In the localization of PCa with MRSI at 3T, the use of the endorectal coil showed a significantly ($P < 0.05$) higher sensitivity (81.3%) than the external phased array (68.8%). In contrast, the specificities of cancer detection were 81% and 75% using the external phased array and the endorectal coils, respectively. Additionally, there was a slight increase in the AUC (86.9%) for endorectal compared to the external phased array AUC (85.9%).

In our investigations using an external phased array coil, the effective voxel size was slightly larger to compensate for the poor SNR compared to examinations of the prostate using an endorectal coil. Overlap exists in the (Ch+Cr)/Cit ratios between cancer and noncancerous tissues. For both ERC and external phased array coils, (Ch+Cr)/Cit ratios were significantly higher in cancer locations than noncancer locations in this study, in accordance with the
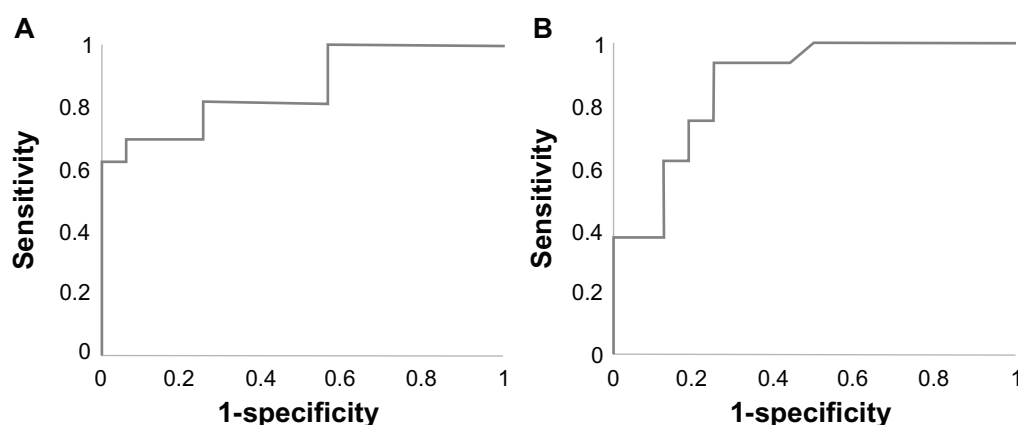

Figure 4. ROC curves of MRSI ratios of prostate cancer patients (**A**) with the endorectal and (**B**) the external phased array 'receive' coils.

Table 2. Measures of sensitivity, specificity, PPV, NPV, and accuracy of endorectal and external body coil MRSI ratios in discrimination of cancer from non-cancer with ROC curve analysis.

Parameter	Endorectal coil	External phased array
CV	1.35	0.77
Sensitivity, %	81.3	68.8
Specificity, %	75.0	81.3
PPV%	76.5	78.6
NPV%	80.0	72.2
AUC, %	86.9	85.9
Accuracy, %	78.1	75.0

Abbreviations: CV, cutoff value; PPV, positive predictive value; NPV, negative predictive value; AUC, area under the curve.

results of previous studies.[21–30] Additionally, the trend of accuracy and sensitivity of the ERC in this study agreed with that of a previous study.[20] The metabolite mean ratio of the external phased array coil was lower in cancer and non-cancer locations due to the low SNR. However, the ratio of (Ch+Cr)/Cit using both coils was generally positively and linearly correlated. Although AUC and sensitivity were elevated for ERC, the results imply that both ERC and external phased-array coil MRS are feasible for detecting the peripheral zone cancer with an optimal threshold ratio for (Ch+Cr)/Cit.

Although the sensitivity and accuracy increased in ERC, there are some disadvantages of using this method. Disadvantages of using an ERC include its invasiveness, image distortions, and a limited field of view. The accuracy of endorectal coil MRI is also frequently affected by image degradation. The three most common causes of this are near-field endorectal surface coil profile (because the coil is close to the gland), phase encoding artifact (from motion of feces or the rectum itself), and incorrect placement of the coil (where the coil is not parallel to the transverse plane of the gland).[31]

Another limitation is the small number of patients in this study. Additionally, there was no correlation between Gleason scores and MRSI ratios. Another limitation of this study was the inclusion of only the peripheral zone of the prostate, in which 75% cancer arises.

Conclusion
These preliminary findings confirmed that the use of ERC significantly improves spectral line width and the coefficient of variance of metabolite ratio compared with the external phased array coil. However, based on overall performance, use of the external phased array coil may be recommended for patients with rectal diseases or patients who could not tolerate the discomfort of endorectal surface coil insertion.

Author Contributions
Conceived and designed the experiments: RN, AT. Analysed the data: RN, DO, MS. Wrote the first draft of the manuscript: RN, AT. Contributed to the writing of the manuscript: DM, RR, SR. Agree with manuscript results and conclusions: RN, DM, SR, AT, MS. Jointly developed the structure and arguments for the paper: RN, AT. Made critical revisions and approved final version: RN, AT, DM, SR, AT. All authors reviewed and approved of the final manuscript.

Competing Interests
Author(s) disclose no potential conflicts of interest.

Disclosures and Ethics
As a requirement of publication author(s) have provided to the publisher signed confirmation of compliance with legal and ethical obligations including but not limited to the following: authorship and contributorship, conflicts of interest, privacy and confidentiality and (where applicable) protection of human and animal research subjects. The authors have read and confirmed their agreement with the ICMJE authorship and conflict of interest criteria. The authors have also confirmed that this article is unique and not under consideration or published in any other publication, and that they have permission from rights holders to reproduce any copyrighted material. Any disclosures

are made in this section. The external blind peer reviewers report no conflicts of interest. Provenance: the authors were invited to submit this paper.

References

1. American Cancer Society. Cancer Facts and Figures 2012. Atlanta, Ga: American Cancer Society; 2012. Availabe at: http://www.cancer.org/acs/groups/content/@epidemiologysurveilance/documents/document/acspc-031941.pdf.

2. Cornel EB, Smits GA, de Ruijter JE, et al. In vitro proton magnetic resonance spectroscopy of four human prostate cancer cell lines. *Prostate*. 1995(5);26:275–80.

3. Kurhanewicz J, Thomas A, Jajodia P, et al. 31P spectroscopy of the human prostate gland in vivo using a transrectal probe. *Magn Reson Med*. 1991;22(2):404–13.

4. Thomas MA, Narayan P, Kurhanewicz J, et al. Detection of phosphorus metabolites in human prostates with a transrectal 31P NMR probe. *J Magn Reson*. 1992;99:377–86.

5. Narayan P, Kurhanewicz J. Magnetic resonance spectroscopy in prostate disease: diagnostic possibilities and future developments. *Prostate Suppl*. 1992;Suppl 4:43–50.

6. van der Graaf M, Schipper RG, Oosterhof GO, Schalken JA, Verhofstad AA, Heerschap A. Proton MR spectroscopy of prostatic tissue focused on the detection of spermine, a possible biomarker of malignant behavior in prostate cancer. *MAGMA*. 2000;10(3):153–9.

7. Bottomley PA. Spatial localization in NMR spectroscopy in vivo. *Ann N Y Acad Sci*. 1987;508:333–48.

8. Brown TR, Kincaid BM, Ugurbil K. NMR chemical shift imaging in three dimensions. *Proc Natl Acad Sci U S A*. 1982;79(11):3523–6.

9. Kurhanewicz J, Vigneron DB, Hricak H, Narayan P, Carroll P, Nelson SJ. Three-dimensional H-1 MR spectroscopic imaging of the in situ human prostate with high (0.24–0.7-cm^3) spatial resolution. *Radiology*. 1996;198(3):795–805.

10. Mescher M, Merkle H, Kirsch J, Garwood M, Gruetter R. Simultaneous in vivo spectral editing and water suppression. *NMR Biomed*. 1998;11(6):266–72.

11. Eilenberg SS, Tartar VM, Mattrey RF. Reducing magnetic susceptibility differences using liquid fluorocarbon pads (Sat Pad): results with spectral presaturation of fat. *Artif Cells Blood Substit Immobil Biotechnol*. 1994;22(4):1477–83.

12. Maio A, Rifkin MD. Magnetic resonance imaging of prostate cancer: update. *Top Magn Reson Imaging*. 1995;7(1):54–68.

13. Kim HW, Buckley DL, Peterson DM, et al. In vivo prostate magnetic resonance imaging and magnetic resonance spectroscopy at 3 Tesla using a transceive pelvic phased array coil: preliminary results. *Invest Radiol*. 2003;38(7):443–51.

14. Fütterer JJ, Scheenen TW, Huisman HJ, et al. Initial experience of 3 tesla endorectal coil magnetic resonance imaging and ^{1}H-spectroscopic imaging of the prostate. *Invest Radiol*. 2004;39(11):671–80.

15. Scheenen TW, Heijmink SW, Roell SA, et al. Three-dimensional proton MR spectroscopy of human prostate at 3T without endorectal coil: feasibility. *Radiology*. 2007;245(2):507–16.

16. Turkbey B, Mani H, Shah V, et al. Multiparametric 3T prostate magnetic resonance imaging to detect cancer: histopathological correlation using prostatectomy specimens processed in customized magnetic resonance imaging based molds. *J Urol*. 2011;186(5):1818–24.

17. Cornfeld DM, Weinreb JC. MR imaging of the prostate: 1.5T versus 3T. *Magn Reson Imaging Clin N Am*. 2007;15(3):433–48.

18. Turkbey B, Pinto PA, Mani H, et al. Prostate cancer: value of multiparametric MR imaging at 3T for detection—histopathologic correlation. *Radiology*. 2010;255(1):89–99.

19. Kim CK, Park BK, Park W, Kim SS. Prostate MR imaging at 3T using a phased-arrayed coil in predicting locally recurrent prostate cancer after radiation therapy: preliminary experience. *Abdom Imaging*. 2010;35(2):246–52.

20. Heijmink SW, Fütterer JJ, Hambrock T, et al. Prostate cancer: body-array versus endorectal coil MR imaging at 3T—comparison of image quality, localization, and staging performance. *Radiology*. 2007;244(1):184–95.

21. Yakar D, Heijmink SW, Hulsbergen-van de Kaa CA, et al. Initial results of 3-dimensional ^{1}H-magnetic resonance spectroscopic imaging in the localization of prostate cancer at 3 Tesla: should we use an endorectal coil? *Invest Radiol*. 2011;46(5):301–6.

22. Kaji Y, Wada A, Imaoka I, et al. Proton two-dimensional chemical shift imaging for evaluation of prostate cancer: external surface coil vs. endorectal surface coil. *J Magn Reson Imaging*. 2002;16(6);697–706.

23. Lichy MP, Pintaske J, Kottke R, et al. 3D proton MR spectroscopic imaging of prostate cancer using a standard spine coil at 1.5 T in clinical routine: a feasibility study. *Eur Radiol*. 2005;15(4):653–60.

24. Kim JK, Kim DY, Lee YH, et al. In vivo differential diagnosis of prostate cancer and benign prostatic hyperplasia: localized proton magnetic resonance spectroscopy using external-body surface coil. *Magn Reson Imaging*. 1998;16(10):1281–8.

25. Coakley FV, Kurhanewicz J, Lu Y, et al. Prostate cancer tumor volume: measurement with endorectal MR and MR spectroscopic imaging. *Radiology*. 2002;223(1):91–7.

26. Carlani M, Mancino S, Bonanno E, et al. Combined morphological, [^{1}H]-MR spectroscopic and contrast-enhanced imaging of human prostate cancer with a 3-Tesla scanner: preliminary experience. *Radiol Med*. 2008;113(5):670–88.

27. Kumar R, Kumar M, Jagannathan NR, Gupta NP, Hemal AK. Proton magnetic resonance spectroscopy with a body coil in the diagnosis of carcinoma prostate. *Urol Res*. 2004;32(1):36–40.

28. Scheidler J, Hricak H, Vigneron DB, et al. Prostate cancer: localization with three-dimensional proton MR spectroscopic imaging–clinicopathologic study. *Radiology*. 1999;213(2):473–80.

29. Shukla-Dave A, Hricak H, Kattan MW, et al. The utility of magnetic resonance imaging and spectroscopy for predicting insignificant prostate cancer: an initial analysis. *BJU Int*. 2007;99(4):786–93.

30. Swindle P, Ramadan S, Stanwell P, et al. Proton magnetic resonance spectroscopy of the central, transition and peripheral zones of the prostate: assignments and correlation with histopathology. *MAGMA*. 2008;21(6):423–34.

31. Hricak H, White S, Vigneron D, et al. Carcinoma of the prostate gland: MR imaging with pelvic phased-array coils versus integrated endorectal-pelvic phased-array coils. *Radiology*. 1994;193(3):703–9.

Multidimensional MR spectroscopic imaging of prostate cancer *in vivo*

M. Albert Thomas[a]*, Rajakumar Nagarajan[a], Amir Huda[a,b],
Daniel Margolis[a], Manoj K. Sarma[a], Ke Sheng[c], Robert E. Reiter[d]
and Steven S. Raman[a]

Prostate cancer (PCa) is the second most common type of cancer among men in the United States. A major limitation in the management of PCa is an inability to distinguish, early on, cancers that will progress and become life threatening. One-dimensional (1D) proton (^{1}H) MRS of the prostate provides metabolic information such as levels of choline (Ch), creatine (Cr), citrate (Cit), and spermine (Spm) that can be used to detect and diagnose PCa. *Ex vivo* high-resolution magic angle spinning (HR-MAS) of PCa specimens has revealed detection of more metabolites such as myo-inositol (mI), glutamate (Glu), and glutamine (Gln). Due to the J-modulation and signal overlap, it is difficult to quantitate Spm and other resonances in the prostate clearly by single- and multivoxel-based 1D MR spectroscopy. This limitation can be minimized by adding at least one more spectral dimension by which resonances can be spread apart, thereby increasing the spectral dispersion. However, recording of multivoxel-based two-dimensional (2D) MRS such as J-resolved spectroscopy (JPRESS) and correlated spectroscopy (L-COSY) combined with 2D or three-dimensional (3D) magnetic resonance spectroscopic imaging (MRSI) using conventional phase-encoding can be prohibitively long to be included in a clinical protocol. To reduce the long acquisition time required for spatial encoding, the echo-planar spectroscopic imaging (EPSI) technique has been combined with correlated spectroscopy to give four-dimensional (4D) echo-planar correlated spectroscopic imaging (EP-COSI) as well as J-resolved spectroscopic imaging (EP-JRESI) and the multi-echo (ME) variants. Further acceleration can be achieved using non-uniform undersampling (NUS) and reconstruction using compressed sensing (CS). Earlier versions of 2D MRS, theory of 2D MRS, spectral apodization filters, newer developments and the potential role of multidimensional MRS in PCa detection and management will be reviewed here. Copyright © 2013 John Wiley & Sons, Ltd.

Keywords: prostate cancer; magnetic resonance spectroscopy; 2D JPRESS; 2D L-COSY; citrate; spermine; echo-planar spectroscopic imaging

INTRODUCTION

Prostate cancer (PCa) is the second leading cause of cancer deaths after lung cancer (1). The most common diagnostic tools used to look for evidence of PCa include digital rectal examination (DRE), serum concentration of prostate specific antigen (PSA) and transrectal ultrasonography (TRUS) guided prostate biopsy (2). The primary system for prognosis of PCa is based on the size and volume of cancer in a prostate biopsy specimen graded microscopically according to the glandular pattern of cancers (Gleason score, GS) (3). The GS is the sum of the two most common patterns (grades 1–5) of tumor growth found. In needle biopsy, it is now recommended that the worst grade should always be included even if present in less than 5% (4). Most PCa lesions are located in the peripheral zone (PZ) of the prostate and may be detected by DRE when the volume is about 0.2 ml or larger (5–7).

Digital rectal examination has a low overall sensitivity (37%) and low positive predictive value (PPV) when lower PSA levels

* Correspondence to: M. A. Thomas, Department of Radiological Sciences, David Geffen School of Medicine, University of California, Los Angeles, CA 90095, USA.
E-mail: athomas@mednet.ucla.edu

a M. A. Thomas, R. Nagarajan, A. Huda, D. Margolis, M. K. Sarma, S. S. Raman
Department of Radiological Sciences, David Geffen School of Medicine, University of California, Los Angeles, CA 90095, USA

b A. Huda
Department of Physics, California State University, Fresno, CA 93740, USA

c K. Sheng
Department of Radiation Oncology, David Geffen School of Medicine, University of California, Los Angeles, CA, USA

d R. E. Reiter
Department of Urology, David Geffen School of Medicine, University of California, Los Angeles, CA, USA

(0–3 ng /ml) are encountered (8). PSA measurement has yielded higher detection rates than DRE (7), but its specificity is low (36%) owing to false-positive PSA elevation under benign circumstances, such as inflammation or benign prostatic hyperplasia (BPH) (9). These inaccurate tools often lead to incorrect diagnoses, inaccurate risk assessments, patient anxiety, and less optimal therapy choices in management of the disease. Hence, there is a need for improved PCa diagnosis with better-detection, localization, and sampling. Prostate cancer is the only major solid organ malignancy that lacks an imaging-based diagnosis.

Diagnostic imaging methods currently in use, such as computerized tomography (CT) and ultrasound (US), cannot adequately detect PCa. MRI offers exquisite anatomical details, but may suffer from poor specificity in detecting and grading PCa (10,11). T_2-weighted (T2W) MRI delineates most larger foci of PCa as a region of low signal intensity surrounded by high signal intensity (longer T_2) of normal PZ tissue (12,13). Although the sensitivity of T2W images for tumor detection is high, specificity is suboptimal (14).

Low specificity may, however, lead to overtreatment, cause great anxiety to patients, and result in many unnecessary biopsies in patients with no or low grade cancers. On the other hand, if the patient with high grade cancer inappropriately chooses "active surveillance" as a management option, malignant cells can metastasize to the other parts of the body before the cancer becomes clinically evident. Thus more sensitive and specific non-invasive tests are needed to better differentiate indolent and aggressive PCa.

Techniques such diffusion-weighted imaging (DWI) and perfusion may improve the performance of MR. DWI is an MRI technique that visualizes molecular diffusion, that is, the Brownian motion of water molecules in biologic tissues (15), by applying two equally sized diffusion-sensitizing gradients, which are characterized by their *b*-values. The mobility is then quantified by calculating the apparent diffusion coefficient (ADC), which depends mainly on the cellularity, cell size, extracellular space, and temperature. When DWI is combined with T2W MRI, both sensitivity and specificity increase substantially. Sensitivity increases from a range of 49–88% for either modality alone to a range of 71–89% with the two modalities combined, while specificity increases from a range of 57–84% to a range of 61–91% (16–18).

Angiogenesis, the formation of new blood vessels, is often associated with malignancy (19,20). A number of studies have reported an increased microvessel density (MVD) in PCa, potentially enabling the detection or localization of tumors through imaging techniques sensitive to these characteristics (21–24). DCE-MRI of PCa is often found to enhance more quickly, to a greater degree, and to show more washout than the benign PZ (22,25–28). Malignant tissue differs from benign tissue with respect to microvessel density, blood flow, vascular morphology and permeability, and flow dynamics (29). A growing body of literature suggests that DCE-MRI may significantly improve cancer detection, tissue characterization, localization, and staging (30–33). According to a study by Kim *et al.*, DCE-MRI has been found to improve accuracy, sensitivity, and specificity by 26%, 31%, and 22% respectively relative to 1.5 T T2W imaging alone (34). Another study by the same group at 3 T also confirmed the superiority of DCE-MRI over T2W imaging (35). However, reports of correlation between DCE-MRI and specific tissue properties such as GS and MVD have been mixed, with both significant (24,36,37) and non-significant (26,38) findings. Moreover, mechanisms governing both qualitative and quantitative changes are not yet fully understood.

MR SPECTROSCOPIC IMAGING OF PROSTATE USING 1D SPECTROSCOPY

MRS is a non-invasive and powerful biochemical technique, which can be performed after the MRI protocol. Four metabolites, namely citrate (Cit), creatine (Cr), spermine (Spm), and choline (Ch) are the ones commonly detected in PCa (39,40). The resonances of the above mentioned metabolites occur at distinct frequencies (approximately 2.6 ppm, 3.03 ppm, 3.1 ppm, and 3.2 ppm, respectively). In healthy prostate tissues, Cit is secreted by the epithelial cells of the prostate in large amounts along with high levels of zinc, which inhibit the oxidation of Cit in the Krebs cycle. In the presence of cancer, the Cit level is dramatically diminished due to significant reduction of zinc in the cancerous epithelial tissue. Concurrently, the Ch level is elevated due to increased cell membrane turnover in the proliferating malignant tissues. Magnetic resonance spectroscopic imaging (MRSI) is promising as a valuable technique for evaluating the extent and aggressiveness of primary and recurrent PCa (10,11). Instead of single voxels, MRSI provides spectra from three-dimensional (3D) spatial arrays of contiguous volumes mapping the entire prostate. MRI and MRSI both are used for detailed anatomic and metabolic evaluations of the prostate. The (Ch + Cr)/Cit ratio is usually used as a criteria for the diagnosis of PCa in the 3D MRSI studies.

A major limitation of the MRSI using 1D spectra is its severe spectral overlap because of limited spectral dispersion at clinically used static magnetic field strengths ($B_0 \leq 3\,T$). Low spectral dispersion causes a large number of metabolites to overlap within a small range of ^1H spectra (0–5 ppm) (41). Consequently, it makes quantification of metabolites very challenging. Further, water and lipid suppression using Mescher–Garwood (MEGA) RF pulses are combined with the localizing point resolved spectroscopy (PRESS) or stimulated echo acquisition mode (STEAM) sequence. This has resulted in a long TE-based MRSI acquisition since the 1990s (10,11,42). Spectral editing techniques (43–47) are generally optimized for detecting one specific metabolite, and hence may not be optimal for simultaneously detecting a large number of metabolites in clinical practice.

SINGLE VOXEL BASED 2D MR SPECTROSCOPY OF PROSTATE CANCER

Different versions of multidimensional techniques have been reported to overcome the signal overlap and to detect several metabolites more unambiguously than conventional MRSI techniques including spectral editing (46–56). Multidimensional MRS enables detection of a larger number of resonances from multiple metabolites with improved spectral resolution than one-dimensional (1D) MRS and a more efficient and accurate identification and quantification of metabolites. There are several books explaining various theoretical aspects of 2D MRS (57–59). Here, we present a brief theoretical explanation to describe the acquisition and post-processing of 2D MRS.

Theory

In the recording of single-voxel-based 1D spectroscopy, once the boundaries of the voxel are spatially localized with slice-selective RF pulses, differences in frequencies of ^1H for different metabolites are attributed to chemical shift or shielding

experienced by the proton in the particular electronic environment and indirect spin–spin coupling (J-coupling) communicated through covalent bonds. Chemical shift results in distribution of signal over several peaks originating from different magnetically non-equivalent proton groups. J-coupling splits the amplitude of each group further, and distributes it over multiplets arising from indirect coupling of magnetically non-equivalent protons mediated by electron–nuclear and electron–electron interactions. Overlap of these multiplets makes quantitation of different metabolites difficult.

2D L-COSY and JPRESS

The idea behind multidimensional spectroscopy is to pry open these interactions and observe their relationships in action. The sequences are designed to see how a spin group modifies its response when another is perturbed in some way. This brings to the foreground the correlation between interacting spin groups, which is the basis of correlated spectroscopy (COSY) (52,57). The three-dimensional (3D) spatially resolved analog of 2D COSY was named "L-COSY" (52). In this scheme, a preparation period initiates a single slice-selective 90° RF pulse or a sandwich of slice-selective RF pulses in two orthogonal planes (90°–Δ–180°–Δ) during which the (longitudinal) equilibrium magnetization of nuclear spins is transferred to transverse magnetization or Hahn spin-echo. This is followed by encoding the second spectral dimension with a *variable* time period, t_1, meaning that, during a series of repeat experiments, t_1 takes on a different set of values. This is usually termed the evolution period, which is then followed by a mixing period containing a slice-selective 90° RF pulse in the third orthogonal plane in 2D L-COSY. During this period, there is a coherence transfer between J-coupled spins. In the localized 2D J-resolved spectroscopy (JPRESS), a slice-refocusing 180° RF pulse replaces the slice-selective 90° RF pulse in the L-COSY sequence (49,50). After this, the data acquisition or detection period, t_2, begins in both L-COSY and JPRESS, during which the digitized signal is recorded as a function of t_2, similarly to 1D MRS. This is repeated several times, creating a 2D data matrix, with each row representing a different t_1. This arrayed signal acquisition, $s(t_2, t_1)$, is the basis of 2D spectroscopy and can be extended to further dimensions by combining with two or three spatially encoding gradients, thereby enabling recording of multivoxel 2D spectra in a single slice or a 3D volume. More spectroscopic dimensions will come into play when considering multinuclear MRS. To understand the nature of the interactions between spins during evolution, mixing, and detection periods, and how these events modulate the amplitude, frequency, phase, and full-width at half maximum (FWHM) of the signal, we need to take a closer look at the J-coupled spin-pair system.

A weakly (or strongly) J-coupled spin pair system is defined as one in which the chemical shift differences between magnetically non-equivalent protons ($\delta_I - \delta_S$) within the molecule are larger than (or equal to/less than) the J-coupling between the spins separated by covalent bonds. It can be shown that a general Hamiltonian for J-coupled spins is given by (58)

$$\hat{H} = \Sigma_j \omega_j I_{jz} + \Sigma_{j<k} 2\pi J_{jk} I_j I_k \qquad [1]$$

where a set of spins (I) with different chemical shifts experiences mutual interactions, and ω and J are expressed in rad/s. For a weakly coupled two-spin system (IS, two spin-½ particles) with four Zeeman product states in superposition, there are four stationary states or energy levels that represent the fractional population of coupled spins at equilibrium. The allowed transitions in a J-coupled

spin pair system are similar to that in an isolated spin system. However, the total magnetic quantum number, m, of only one spin can change by ±1. Hence, there will be four resonances containing two doublets for the IS protons with one for the I and the other for the S spin.

2D L-COSY

The 2D signal from spin I acquired along the detection dimension (t_2) is given by (52)

$$s(t_1, t_2) = \mathrm{Tr}[(I_x)\sigma]\exp\left(-i\omega_2^{(I)}t_2\right)\exp(-t_1/T_2)\exp(-t_2/T_2)[1 - \exp(-T_R/T_1)]$$

[2]

where

$$\sigma \propto -0.5\cos(2\pi J\Delta)[I_y\cos(\omega_1^{(I)}t_1)\cos(\pi Jt_1) + I_x\sin(\omega_1^{(I)}t_1)\cos(\pi Jt_1)$$

$$+2I_zS_x\cos(\omega_1^{(I)}t_1)\sin(\pi Jt_1) - 2I_zS_y\sin(\omega_1^{(I)}t_1)\sin(\pi Jt_1)]$$

$$+0.5\sin(2\pi J\Delta)[I_y\cos(\omega_1^{(I)}t_1)\sin(\pi Jt_1) + I_x\sin(\omega_1^{(I)}t_1)\sin(\pi Jt_1)$$

$$-2I_zS_x\cos(\omega_1^{(I)}t_1)\cos(\pi Jt_1) + 2I_zS_y\sin(\omega_1^{(I)}t_1)\cos(\pi Jt_1)]$$

[3]

T_R, T_1, and T_2 represent repetition time and longitudinal and transverse relaxation times, respectively. It is also evident from Equation [3] that the coherence transfer (CT) from spin I to S is characterized by two-spin operators, $2I_zS_x$ and $2I_zS_y$. A similar equation can be derived for S spin resulting in a coherence transfer to I spin.

Apodization filters for 2D L-COSY

As shown in Equation [3], the first maximum of the CT echo will occur at $t_1 = 1/2J$ for the two-spin system (IS) and the position of the maximum for lactate (I_3S, three methyl and one methine protons) will be at $t_1 = \pi/4J$ as described previously by Ziegler *et al.* (60). In a strongly coupled AB spin system such as citrate in the prostate, the coherence transfer function becomes more complicated, since the chemical shift difference is equal to or less than J (50,54,61). It is also evident in Equations [2] and [3] that the 2D diagonal peak intensities follow a cosine dependence and time domain cross-peak amplitudes increase from zero at the beginning to a maximum at $1/2J$ with the signal decay according to T_2^*. As discussed by Ernst *et al.*, for small t_1 and t_2 values, the contribution to the 2D cross peak volume is insignificant (57). Hence, it is advisable to weight the time-domain signal, as shown in Equation [2], by a weighting function that will deemphasize the signal for small t_2 and t_1 values (57). While post-processing a 2D L-COSY spectrum, optimal matching filters such as a sine-bell or skewed squared sine-bell can be used along both dimensions for better sensitivity of 2D cross peaks. A sine-bell (SB) filter can be defined as

$$SB_n = \sin\left\{(\pi/n)\left[1 + (n-1)t_w/\left(t_i^{max} - t_i^{min}\right)\right]\right\} \qquad [4]$$

where n being the shift parameter is a positive integer and i runs over the two dimensions, 1 and 2. For large n, Equation [4] reduces to

$$SB = \sin\left\{\pi t_w/\left(t_i^{max} - t_i^{min}\right)\right\} \qquad [5]$$

As shown in Equation [5], the symmetric unshifted SB function has a maximum value of 1 at $t_w = (t_i^{max} - t_i^{min})/2$.

As the maximum value can be reached at an earlier time, the shifted SB or its square (SB_n^2) may offer more flexibility than the unshifted ones.

As described by Delikatny *et al.* (62), there are three major advantages with using the SB filter. (1) As it begins with zero value, unlike an exponential filter, it can emphasize cross peaks relative to 2D diagonal peaks that are cosine dependent. (2) It removes the broad wings (dispersive components) from 2D magnitude lineshapes. (3) At the end of the time domain, the trailing edge of the SB function the window function goes smoothly to zero and truncation errors due to apodization are minimized.

Shown in Figure 1(A) is a 2D L-COSY spectrum recorded in the peripheral zone of a 28 y.o. healthy prostate using a 1.5 T whole body MRI/MRS scanner (GE Medical Systems, Waukesha, WI) with an endorectal coil (MEDRAD, Pittsburgh, PA) combined with a pelvic phased-array coil for signal reception. A body RF coil was used for transmitting the RF pulses. A $2 \times 2 \times 1$ cm^3 voxel was placed on the lower left peripheral zone using an axial fast spin-echo MRI. The 2D L-COSY spectrum was recorded using the following parameters: $T_R = 2$ s, minimal $T_E = 30$ ms, 45 t_1 increments and 16 averages. The total acquisition time was 24 min. The raw data was acquired using 1024 complex points and a spectral window of 2500 Hz along the detected direct (t_2) dimension. The incremental period (Δt_1) was 1.6 ms to yield a spectral window of 625 Hz along the second indirect dimension (t_1). The spectral 2D raw files were processed using the FELIX software package (Felix NMR Inc., San Diego, CA). The 2D MRS array was apodized using the skewed squared sine-bell filters (62) along the two axes and before zero-filling to 2048×256. After double Fourier transformation, the 2D L-COSY spectra were reconstructed in the magnitude mode and displayed as contour plots. For comparison, shown in Figure 1B is the same 2D L-COSY data processed using the conventional exponential filter functions (3 Hz), where the emphasis of discriminating 2D cross peaks from the diagonal peaks is completely sacrificed compared with the skewed squared sine-bell filters.

2D JPRESS

In the half-echo sampled 2D JPRESS, two increments ($t_1/2$) are used before and after the last 180° RF pulse (49,50). The 2D signal for spin *I* acquired along the detected dimension (t_2) is the same as shown in Equation [2] with a redefined σ and ω_1. As there is no mixing period here, the 2D JPRESS spectrum contains the same number of peaks as the conventional 1D MRS using the PRESS sequence. The second spin-echo during which the second spectral dimension is encoded will refocus the chemical shift but not in bilinear interaction, *J*, similar to the first Hahn echo. The frequency of each peak along the t_1 dimension will be dependent on *J* only, where the frequency along the t_2 dimension will be (chemical shift $\pm 1/2$ *J*). A more detailed theoretical explanation is discussed by Thrippleton *et al.* (63).

2D JPRESS of a healthy human prostate

Figure 2(B) shows a 2 ml voxel 2D JPRESS spectrum of the same 28 y.o. healthy prostate as shown in Figure 1. The voxel location of the 2D JPRESS spectrum is shown in Figure 2(A). The 2D peaks due to Cit were located along $F_1 = \pm 1.6$ Hz, ± 7.9 Hz, and ± 17.5 Hz. In addition, the triplet nicely resolved about $F_2 = 3.1$ ppm along $F_1 = 0$ Hz and ± 7.8 Hz was identified as Spm. The presence of strong Cit peaks was consistent with the well-known fact of its high abundance in healthy prostate (39,40). Moreover, there were 2D peaks along $F_1 = 0$ Hz due to Cr and Ch at $F_2 = 3.0$ ppm and 3.2 ppm, respectively. The J-resolved peaks due to Ch methylene protons were not observable due to the smaller voxel size and reduced number of averages.

Apodization filters for 2D JPRESS

The J-coupled multiplets are better resolved along the t_1 dimension than the detected t_2 dimension as well the 1D MRS counterpart, since any defocusing linear B_0 interactions including the static field inhomogeneities during the first half of t_1 are
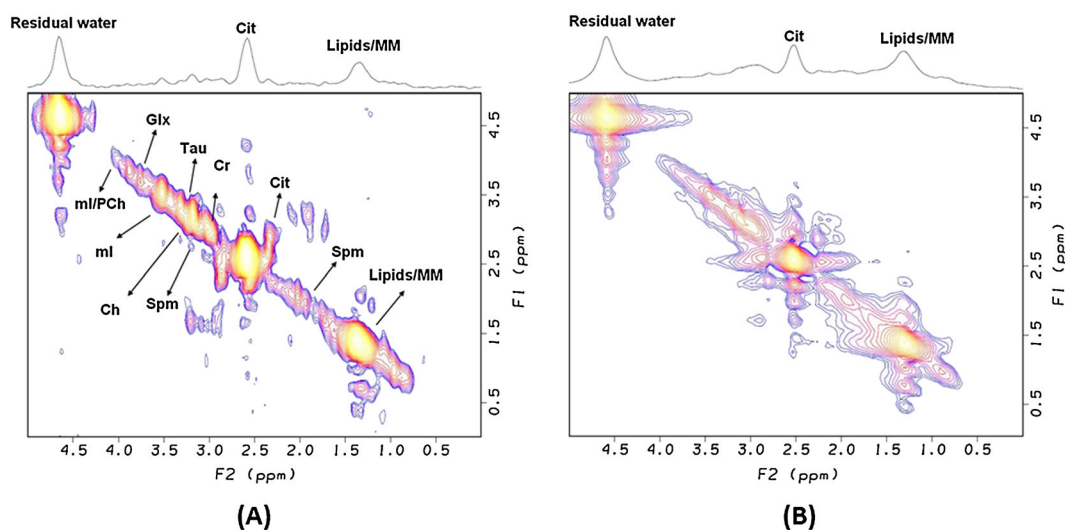

Figure 1. A 1.5 T 2D L-COSY spectrum recorded from a healthy prostate of a 28 y.o. male using two different apodization filters: (A) a skewed squared sine-bell and (B) an exponential filter using a 3 Hz line broadening. The 2D L-COSY spectrum was recorded using the following parameters. A $2 \times 2 \times 1$ cm^3 voxel was placed on the lower left peripheral zone, $T_R = 2$ s, minimal $T_E = 30$ ms, 45 t_1 increments, incremental period (Δt_1) of 1.6 ms to yield a spectral window of 625 Hz along the F_1 dimension, 16 averages per Δt_1, 1024 complex points and a spectral window of 2500 Hz for the F_2 dimension. The total acquisition time was 24 min. An endorectal coil combined with a pelvic phased-array coil for signal "receive" and a body rf coil for "transmit" were used. The raw spectral files were processed using the FELIX software package (Felix NMR Inc., San Diego, CA). After zero-filling to 2048×256, double Fourier transformation was performed and the 2D L-COSY spectra were reconstructed in the magnitude mode and displayed as contour plots.
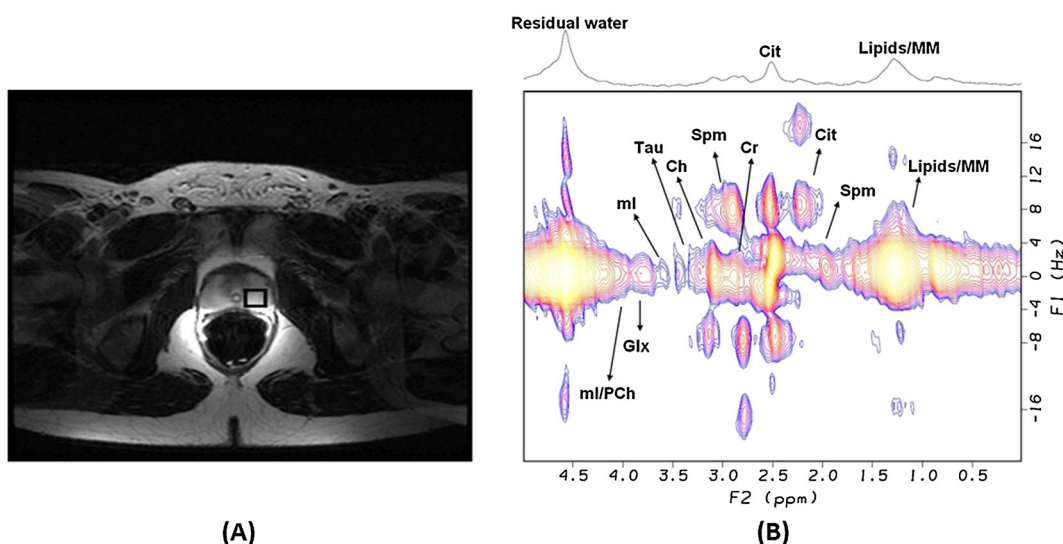
Figure 2. (A) An axial fast spin-echo MRI slice showing the 2D MRS voxel; the MRI acquisition parameters were as follows: 4 mm slice, $T_R = 2.5$ s, $T_E = 84$ ms, FOV = 14–24 cm, acquisition matrix 256×192, and 4 number of excitations (NEX), resulting in an acquisition time of 4 min. (B) A half-echo sampled 1.5 T 2D JPRESS spectrum recorded in the peripheral zone of the same 28 y.o. healthy prostate as used for Figure 1 using the following parameters: $2 \times 2 \times 1$ cm^3 voxel, $T_R = 2$ s, minimal $T_E = 30$ ms, 45 t_1 increments, incremental period (Δt_1) of 10 ms (5 ms before and 5 ms after the last 180° RF pulse) to yield a spectral window of ± 50 Hz along the F_1 dimension, 16 averages per Δt_1, 1024 complex points and a spectral window of 2500 Hz for the F_2 dimension. The total acquisition time was 24 min.

refocused during the second half, resulting in a net zero dependence on the B_0 static field inhomogeneities and other linear interactions. Even though this is a major advantage, the phase-modulated time domain datasets are transformed into phase-twisted 2D peaks after the double fast Fourier transformation (FFT) of the 2D JPRESS raw data. Hence, the above mentioned squared or simple sine-bell filter functions can be used prior to the double FFT.

Strong coupling effects in 2D JPRESS

It was demonstrated earlier that 2D JPRESS spectra of brain and prostate metabolites show more cross peaks than those of weakly coupled ones (50,54). Shown in Figure 3 is a simulated hard pulse version of the 2D JPRESS (90°–180°–180°) spectrum of Cit using the GAMMA simulation library (64). Cit has two equivalent methylene groups. Each proton pair forms a strongly J-coupled AB spin system (50,54), resulting in eight J-resolved 2D peaks anti-symmetric about $F_2 = 2.65$ ppm, as evident in the experimental and simulated 2D spectra. The 2D peaks located along $F_1 = \pm 1.6$ Hz, ± 7.8 Hz, and ± 16.4 Hz were in agreement with a previous report (54). Besides, the projected 1D spectra onto F_1 and F_2 axes are also shown.

2D JPRESS of PCa patients with two different Gleason scores (GS)

Figure 4 shows 2D JPRESS spectra recorded in a 59 y.o. BPH and a 50 y.o. PCa patient using a Siemens 1.5 T Avanto MRI scanner. The metabolites such as Cit, Ch, Cr, and Spm were identified and the 2D multiplet patterns of Cit and Spm in JPRESS spectra were detected with a reasonable resolution. However, the limited spectral resolution along the second axis (F_1) resulted in an overcrowded 2D JPRESS spectrum. This complex spectrum is due to the strong coupling effects of Cit as presented in Figure 3. Nagarajan et al. (56) have shown a decrease of Spm in PCa patients of higher GS (4+3) compared with lower GS
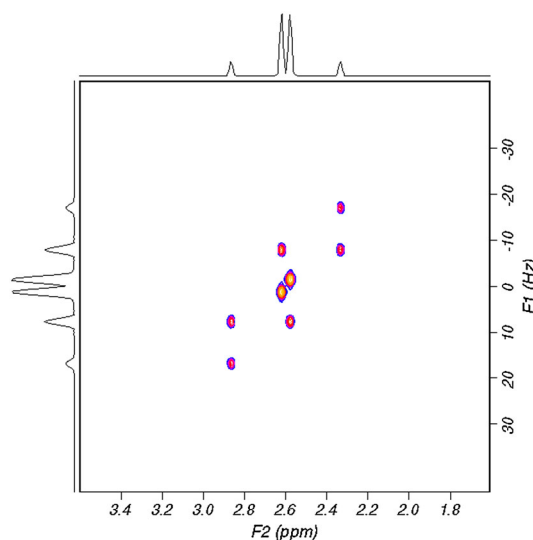

Figure 3. A simulated 1.5 T 2D JPRESS spectrum of citrate using $J = 15.6$ Hz and $\delta = 9.6$ Hz at 1.5 T ($T_R = 2$ s, $T_E = 30$ ms, 256 F_1 points, and 4096 F_2 points).

(3+4) using 2D J-resolved spectroscopy. High levels of Spm are found in the healthy prostatic ducts (65–67) and the observed variations of Spm in cancer may be due to the loss of ductal morphology or a reduction in the secretion of polyamines (68). The Spm itself, which plays a role in cell proliferation and differentiation, may provide additional information for early diagnosis and prognosis predicting tumor progression. However, the separation of Ch from Spm is inherently difficult because of the proximity of the peaks and the limited spectral resolution available within a reasonable imaging time. A distinct integration region cannot be assigned for Spm. Thus, polyamine level could not be integrated and quantified unambiguously using operator
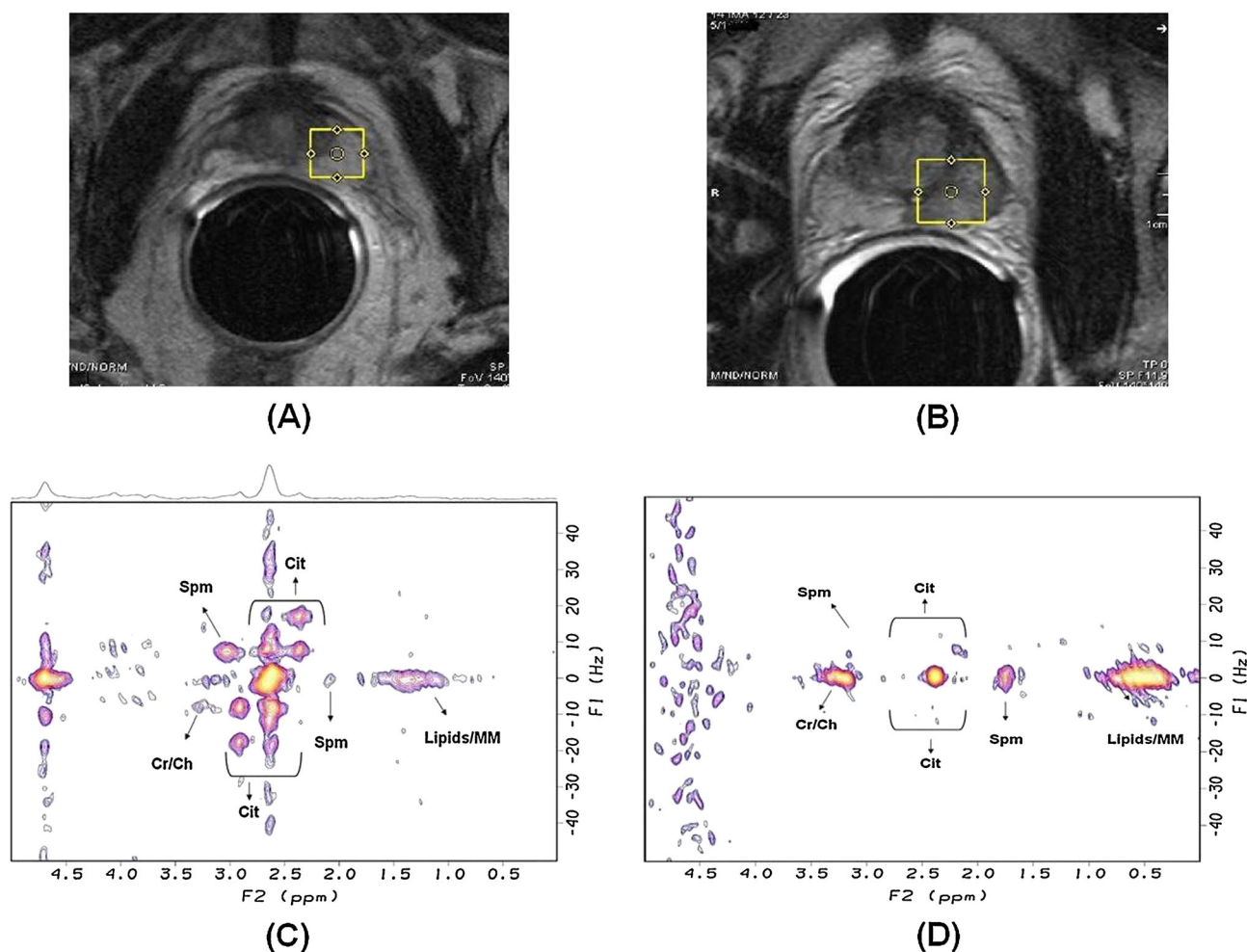
NMR Biomed. (2013)
wileyonlinelibrary.com/journal/nbm

Figure 4. T_2-weighted axial MRI slice images showing locations of 2D JPRESS spectra recorded in the peripheral zones of (A, C) a 59 y.o. BPH patient and (B, D) a 50 y.o. prostate cancer patient. The half-echo sampled 2D JPRESS spectra were recorded using the following parameters: a 1.5 T MRI scanner, $T_R = 2$ s, minimal $T_E = 30$ ms, 64 t_1 increments, incremental period (Δt_1) of 10 ms (5 ms before and 5 ms after the last 180° RF pulse) to yield a spectral window of ±50 Hz along the F_1 dimension, eight averages per Δt_1, 2048 complex points and a spectral window of 2000 Hz for the F_2 dimension. The total acquisition time was 16 min. The raw spectral files were processed using the FELIX software package (Felix NMR Inc., San Diego, CA). After zero-filling to 2048 × 256, double Fourier transformation was performed and the 2D JPRESS spectra were reconstructed in the magnitude mode and displayed as contour plots.

defined peak volumes in the frequency domain. It can be only assessed qualitatively and reported relative to the choline peak. In the prostate, Spm has three multiplets at 1.8 ppm, 2.1 ppm, and 3.05–3.15 ppm. The 3.05–3.15 ppm multiplet occurs between the Cr and Ch singlets and cannot be entirely resolved from them. Although this ratio has been traditionally called the (Ch+Cr)/Cit ratio, it actually includes Spm also. This presents a problem when Ch is elevated in cancer and Spm is diminished. This hinders accurate quantification of both metabolites. Application of localized 2D JPRESS was also reported in prostate *in vivo* studies by another group (69).

Maximum-echo sampled 2D JPRESS

In the half-echo sampled 2D JPRESS, if the incremental period (Δt_1) typically used is 10 ms, the resulting total echo time duration will be 630 ms to achieve a spectral window of 100 Hz along F_1. This would lead to severe T_2 attenuation of 2D peaks, resulting in a significant signal loss. It is known that T_2 value of several metabolites are shorter at 3 T than 1.5 T (70,71), which

would lead to further attenuation of J-resolved 2D peaks at higher field strength. As reported by Schulte *et al.* recently, a maximum-echo based JPRESS can sample the echo signals starting immediately after the final crusher gradient of the last 180° pulse (72). This acquisition scheme has several advantages over the half-echo sampling data presented in the previous section, where the acquisition starts at the echo top.

A common definition of the sensitivity is the signal-to-noise (SNR) ratio per unit time for identical experimental durations and a constant acquisition time window; the noise will remain the same and it is sufficient to compare the signal. The signal is commonly defined as the peak height in the frequency domain, which is equivalent to the integral of the time domain signal. For single resonances, it suffices to integrate over the exponential damping curve of the echo along the times t_1 and t_2.

As described by Schulte *et al.*, the efficiency of 2D experiments can be compared with 1D PRESS by integrating over the indirect dimension (t_1). The maximum-echo sampled JPRESS signal can be divided into two halves (72). The damping curve in the traditional half-echo sampling JPRESS is equivalent to the right

half as shown in the following equation:

$$\int^{T_{s1}}\int^{\infty}\exp(-t_2/T_2^*)\exp(-t_1/T_2)\,dt_2dt_1$$
$$= T_2^*T[1 - \exp(-T_{s1}/T_2)] \qquad [6]$$

where T_{sl} represents the total sampling time along t_1.

Adding both halves together, the total signal of the maximum-echo sampled JPRESS can be written as

$$2T_2^*T_2[1 - \exp(-T_{s1}/T_2)] - T_2^*t_x[1 - \exp(-T_{s1}/t_x)] \qquad [7]$$

where

$$t_x = 2T_2T_2^*/(T_2 + 2T_2^*) \qquad [8]$$

In contrast, the equation for the 1D PRESS sequence with the shortest TE equivalent to the 2D JPRESS at $t_1 = 0$ can be written as the following:

$$\int^{T_s}\int^{\infty}\exp(-t_2/T_2^*)\,dt_2dt_1 = T_2^*T_{sl} \qquad [9]$$

The ratio of maximum-echo sampled JPRESS to PRESS is given by

$$2T_2/T_{s1}[1 - \exp(-T_{s1}/T_2)] - t_x/T_{s1}[1 - \exp(-T_{s1}/t_x)] \qquad [10]$$

and half-echo JPRESS to PRESS (Equation [9]) by

$$T_2/T_s[1 - \exp(-T_{sl}/T_2)] \qquad [11]$$

As presented by Schulte *et al.*, the maximum-echo sampled JPRESS scheme has optimal sensitivity in 2D experiments and it has the same sensitivity as the 1D PRESS at long $T_2 > 200$ ms, which is the case for singlets from Cr and trimethyl protons of Ch (72).

Shown in Figure 5 is maximum-echo sampled 2D JPRESS data acquired in a 27 y.o. healthy male before (A) and after (B) a phase rotation using the following parameters: a voxel of $2 \times 2 \times 2$ cm^3, $T_R/T_{Emin} = 2$ s/30 ms, 2048 complex points for the detected t_2 dimension sampling a spectral width of 2000 Hz, 100 Δt_1 increments before the last 180° slice-selective RF pulse with each $\Delta t_1 = 1$ ms, eight averages per Δt_1, a 3 T MRI scanner, 16 channel body matrix coil for "receive" and a quadrature body "transmit" coil. This is in agreement with what was shown by Lange *et al.* (69).

ECHO-PLANAR CORRELATED AND J-RESOLVED SPECTROSCOPIC IMAGING

The single-voxel (SV)- based 1D and 2D MRS studies suffer from limited spatial coverage due to recording of one voxel per measurement. In contrast, the 2D or 3D MRSI technique would facilitate adequate spatial coverage in a single recording. However, a major limitation of the conventional 2D/3D MRSI technique stems from using incremented phase encoding for two or three directions to traverse the *k*-space and the total scan time required for the acquisition of a high-resolution 3D MRSI data may be prohibitively long for clinical exams. Another drawback is that only four major metabolites (Cit, Cr, Spm, and Ch) have been detected by the 3D MRSI sequence due to long T_E for optimal suppression of water and lipids. The acquisition of fully phase-encoded MRSI can be greatly shortened by using echo-planar spectroscopic imaging (EPSI), a method originally proposed by Mansfield (73), in which a time varying readout gradient encodes spatial and spectral dimensions during a single readout. Much effort has been devoted to implementing EPSI (74–78), the results of which have shown sufficient SNR. In the last few years, two different fast MRSI sequences have been demonstrated with potential applications in PCa. First, the flyback echo-planar read-out trajectories were incorporated by Chen *et al.* into the PRESS sequence using composite RF pulses with high-quality MRSI data recorded in nine PCa patients (79). Second, high-resolution EPSI was implemented on a 4.7 T MRI scanner with the sequence tested in animal models of PCa (80).

To overcome a major limitation of the SV localized 2D MRS, phase-encoding gradients can be combined with L-COSY and JPRESS to record multivoxel 2D spectra in human tissues. However, the total duration will be impractically long due to four different increments for encoding: one for the second spectral dimension and three for the three spatial dimensions. With the above mentioned progress in accelerating one spatial and
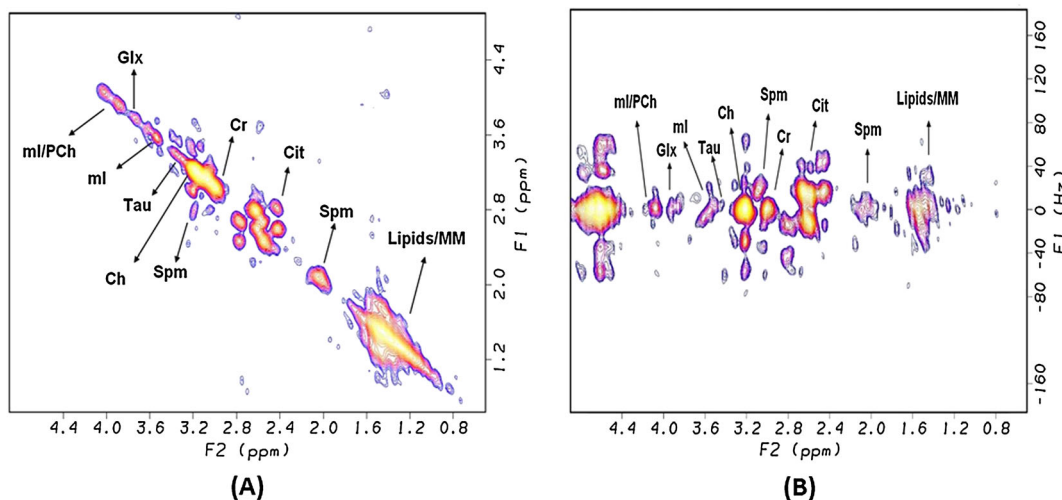

Figure 5. A maximum-echo sampled 2D JPRESS spectrum recorded in the peripheral zone of A 27 y.o. healthy prostate using a 3 T MRI scanner after (A) a double FFT of the 2D raw matrix and (B) a double FFT after incorporating the phase rotation of the raw matrix to impose the evolution after the last 180° slice-selective RF pulse.

spectral coverage using the 3D EPSI, the 2D L-COSY and JPRESS sequences were recently modified with an EPSI type of readout to yield 2D spectra from multiple voxels in a single experiment, called echo-planar correlated spectroscopic imaging (EP-COSI) (81) and echo-planar J-resolved spectroscopic imaging (EP-JRESI) (82), respectively. The EP-COSI and EP-JRESI sequences use a bipolar spatial read-out train facilitating simultaneous spatial and spectral encoding, and the conventional phase and spectral encodings for the remaining spatial and indirect spectral dimensions. Multiple 2D COSY and 2D J-resolved spectra were recorded over the spatially resolved volume of interest (VOI) localized by a train of three slice-selective RF pulses (90°–180°–90°) and (90°–180°–180°). These two techniques can be used to detect and quantify metabolites with less T_2 weighting than the earlier 3D MRSI sequences using conventional phase encoding because of the shorter echo time. Figure 6 shows the four-dimensional (2D spectral + 2D spatial) EP-COSI data recorded in a 27 y.o. healthy volunteer. The voxel placement is shown in Figure 6(A) and the multivoxel display of Cr, Ch, and Spm over the localized VOI in Figure 6(B). An extracted 3 ml 2D COSY spectrum is displayed in Figure 6(C).

A 500 ml prostate phantom was prepared containing the following metabolites at physiological concentrations as reported in healthy human prostate (69): Cit (50 mM), Cr (5 mM), Ch (1 mM), Spm (6 mM), mI (10 mM), PCh (2 mM), taurine (Tau, 3 mM), Glu (4 mM), Gln (2.5 mM) and scyllo-inositol (Scy, 0.8 mM). Here, we show that all of the above mentioned metabolites can be detected using fully encoded EP-JRESI data. Shown in Figure 7(A) is an axial MRI slice image showing the multivoxel grids of MRSI with the yellow boundary of the field of view (FOV), and the white box representing the volume of interest (VOI) localized by the PRESS sequence which is an integral part of the EP-JRESI sequence (82). The following parameters were used for acquiring the 4D EP-JRESI data: $T_R/T_E =$ 1500 ms/30 ms, 16 phase encodes (k_y), 32 read-out points (k_x) with oversampling, 512 ± read-out trains resulting in 512 pairs of complex spectral points in the second spectral dimension (t_2), 100 t_1 increments for the indirect spectral dimension and one average per encoding. A total duration of 40 min was necessary to acquire this water-suppressed 4D EP-JRESI data. A non-water-suppressed EP-JRESI data using four averages with only one t_1 increment was used for eddy current and phase correction of the suppressed data (81). After apodization and Fourier transformation of this 4D data, the reconstructed 2D J-resolved spectra were overlaid on top of

the 16×16 spatial grids. An extracted 2D J-resolved spectrum (3 ml) around the center of the VOI is shown in Figure 7(B). The diagonal peaks cutting through $F_1 = 0$ show all singlets contained in a 1D PRESS spectrum and the 2D cross (off-diagonal) peaks of J-coupled metabolites such as Cit, Spm, Glu, Gln, and mI were also clearly visible.

MULTI ECHO (ME) BASED ECHO-PLANAR J-RESOLVED SPECTROSCOPIC IMAGING (MEEP-JRESI)

Multi-echo (ME) encoding schemes, namely turbo spin echo (TSE) and fast spin echo (FSE), have been shown to decrease the overall scan time in MRI (83–85). Similar approaches have demonstrated the applicability of ME techniques to MRSI (86,87). One limiting factor for ME-based MRSI is the T_2 decay as the signal is greatly diminished with each echo, especially in living tissues, where T_2 relaxation times are shorter (70,71,88). Recently, a 4D EP-JRESI sequence was implemented combining two spectral dimensions with two spatial dimensions and incorporating multi-echo (ME) for encoding one of the spatial dimensions to reduce scan times to suit clinical requirements. Nagarajan *et al.* (89) employed the MEEP-JRESI sequence on a 3 T MRI/MRS scanner and evaluated it in three healthy prostate volunteers using the external body matrix "receive" coil. The MEEP-JRESI technique facilitates recording multivoxel 2D J-resolved spectra in a single recording using a total acquisition time of approximately 13 min. Figure 8(A) shows the T_2-weighted axial MRI displaying the VOI location for the MEEP-JRESI recorded in a 28 y.o. healthy volunteer. A multivoxel display of Cr/Ch/Spm inside the VOI is shown in Figure 8(B) with each voxel resolution of 2 ml.

4D EP-JRESI AND EP-COSI: ACCELERATED ACQUISITION AND COMPRESSED SENSING RECONSTRUCTION

Image acquisition approaches have conventionally followed the Nyquist–Shannon sampling theorem, where the sampling rate
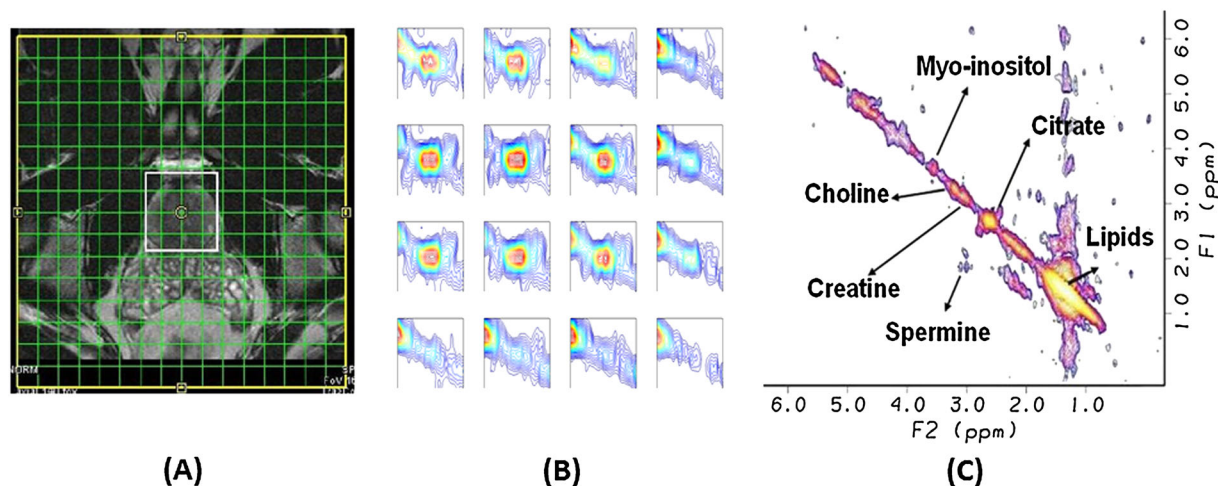

(A)   (B)   (C)

Figure 6. (A) T_2-weighted axial MRI of 27 y.o. healthy volunteer with MRSI voxel location using a 3 T MRI scanner and (B) multivoxel distribution of Cr, Ch, and Spm peaks extracted from the EP-COSI data. (C) 2D L-COSY spectrum extracted from the EP-COSI data of a 27 y.o. healthy male.
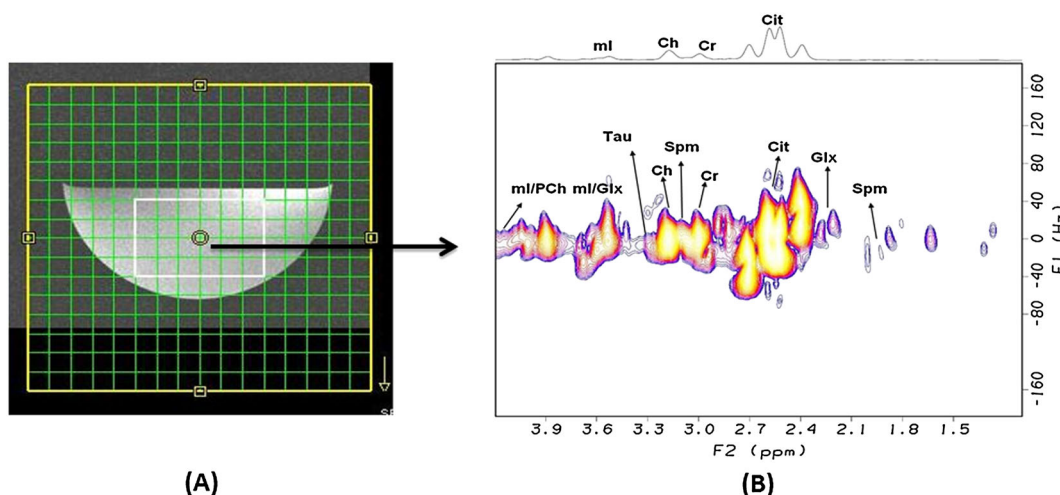
Figure 7. (A) An axial slice MRI of a prostate phantom containing 10 metabolites; (B) an extracted 2D J-resolved spectrum (voxel size of 3 ml). A 3 T MRI scanner was used.
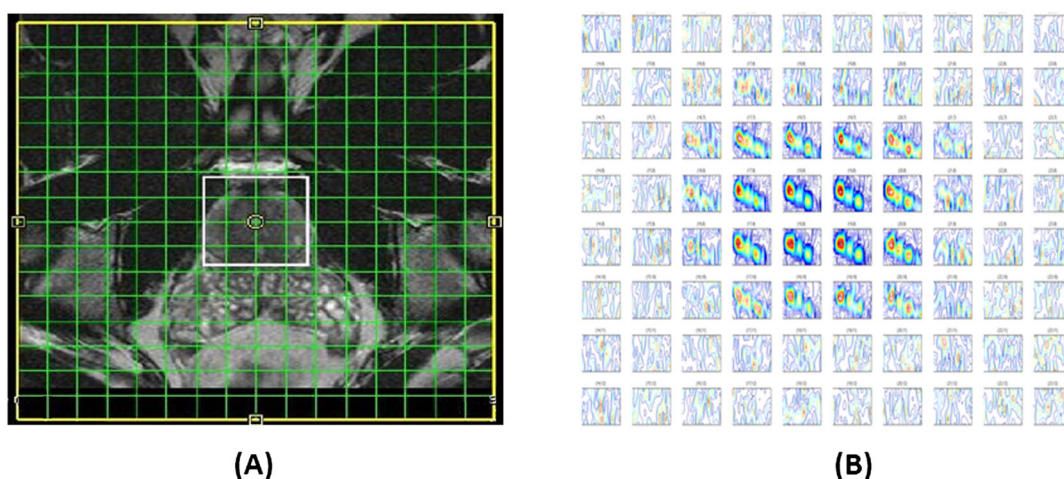

Figure 8. (A) The T_2-weighted axial MRI and (B) multivoxel distribution of Cr, Ch, and Spm from a 28 y.o. healthy prostate from MEEP-JRESI. A 3 T MRI scanner was used.

should be at least twice the maximum frequency present in the signal of interest. However, the theory of compressive sensing (CS) describes a combined sampling and reconstruction paradigm which states that certain images and signals can be recovered from an acquisition that uses fewer samples than required by Nyquist–Shannon (90,91). Since the annual meeting of the International Society for Magnetic Resonance in Medicine in May 2007, CS has met with significant enthusiasm among MR researchers (92–96). Three criteria are critical for the successful application of CS (92): (1) the data should have a sparse representation in a particular transform domain, (2) the aliasing from undersampling should be incoherent in that transform domain and (3) a nonlinear reconstruction should be used to enforce both the sparsity of the reconstruction and consistency with the measurements. MRI is well suited for CS, and there are significant benefits in imaging speed and reduced costs, thereby improving patient care. A major challenge in designing CS data acquisition methods for MRI is in implementing NUS densities that result in incoherent aliasing while providing data sparsity in a transform domain, such as wavelets, curvelets, etc (76). Incoherent aliasing combined with sparsity in the transform domain allows L1-norm-based reconstructions from NUS data to be exact under ideal conditions and "approximately" exact under normal conditions (90,91). Application of CS sampling and reconstruction has been accomplished in parallel imaging to exploit both image sparsity and coil sensitivity encoding (97). As described earlier, there are three spatial encodings and one spectral encoding in a 3D MRSI sequence, and recently Vigneron and co-workers developed an undersampling scheme along both spatial encoded dimensions to achieve suitable incoherent aliasing. They have demonstrated a factor of two enhancement in the spatial resolution without increasing acquisition time or decreasing coverage (94). A further modified scheme was shown to provide up to a acceleration factor of 7.5 for hyperpolarized MRSI (98).

The total duration of a fully encoded 3D MRSI can be approximately 2 hours if the following parameters are used: $T_R = 1\,s$, $12 \times 12 \times 12$ for phase-encoding along three spatial dimensions and four averages. Therefore, average weighted and other schemes have been used to minimize the total time (99). During the last five years, two different fast MRSI sequences have been demonstrated for PCa as mentioned earlier (79,80). There has

been one report of combining two spectral dimensions with 2D spatial encoding applicable to PCa (100). As discussed earlier, a second spectral dimension was added to the EPSI technique in the recently published 4D EP-COSI sequence (81). A total scan time of 40 min was required for 512×100 complex points along the two spectral dimensions with a 16×16 spatial resolution along the two spatial dimensions.

We demonstrate here that by imposing a NUS scheme on the above presented fully sampled data shown in Figure 7(B) and after the CS reconstruction, the quality of the extracted 2D MRS spectra from the undersampled data is comparable to that of the fully sampled data. Therefore, NUS was imposed on one spectral and one spatial dimension and the remaining spectral and spatial dimensions were fully sampled by the EPI readout. Compared with the fully encoded data, the 25% NUS densities demonstrate 4× undersampling, which reduced total scan duration to 10 min. Figure 9 shows the multivoxel EP-JRESI data (A) and extracted 2D J-resolved spectrum (B) after the CS reconstruction, demonstrating the fidelity of the CS reconstruction.

The feasibility of recording a 25% sparsely sampled *in vivo* EP-JRESI data and successful CS reconstruction of the 2D J-resolved spectrum is demonstrated here. A 32 y.o. healthy human subject was investigated on the 3 T MRI scanner using the quadrature body coil "transmit" and external body matrix "receive" coil assembly. The following parameters were used to acquire the NUS sampled EP-JRESI data: $T_R/T_E = 1.5$ s/30 ms, 2 averages, $512 t_2$, oversampled 32 k_x, 25% NUS along the indirect spectral (t_1) and spatial k_y dimensions. In Figure 10(A), an axial MRI of the abdomen is shown displaying the VOI covering the prostate localized by the PRESS sequence and the EP-JRESI grids. The split-Bregman iterative algorithm (101) was used to reconstruct the missing t_1 and k_y data points from the prospectively undersampled data matrix. The CS-reconstructed multivoxel display confirmed the feasibility of detecting prostate metabolites over many voxels. The CS-reconstructed 2D J-resolved spectrum extracted from the central location is shown in Figure 10(B). The 2D diagonal and cross peaks of Cit and other metabolites are visible as reported in a recent publication (102). The endorectal "receive" coil is expected

to facilitate at least one order of magnitude higher sensitivity than that of the body matrix assembly used here. Hence, significantly improved sensitivity can be achieved using the endorectal coil. Our recent findings on the endorectal coil-based NUS EP-JRESI acquisition and CS reconstruction confirming the improved detectability of prostate metabolites will be published elsewhere.

PRIOR-KNOWLEDGE FITTING FOR QUANTITATION OF PROSTATE METABOLITES

As discussed earlier, previous attempts by other researchers using the single- and multivoxel-based 1D MRS approaches have reported four prostate metabolites only, such as Cit, Ch, Spm, and Cr (10,11). This was due to the long echo time ($T_E > 100$ ms) and limited 1D spectral quantitation approaches used. Recent investigations of HR-MAS of *ex vivo* prostate cancer specimens on ultra-high field NMR spectrometers have demonstrated quantitation of many more metabolites such as Tau, mI, scyllo-inositol (sI), Glx, etc. than what has previously been shown using the 1D MRS *in vivo* approaches so far (103–105). A recent report has used prior-knowledge-based LC-model processed HR-MAS *ex vivo* data to quantify additional metabolites such as Glx and glucose (106). A few years ago, Schulte *et al.* developed a prior-knowledge fitting (ProFit) algorithm and demonstrated the feasibility of quantitation of brain and prostate metabolites (69,72,107). After the fitting process, the quality of the fit can individually be evaluated for each metabolite using Cramér–Rao lower bounds (CRLB) (108). A statistical lower bound for the achievable standard deviation of the estimated parameters is provided by CRLB which are not dependent on the individual concentrations but only on the noise and the orthogonality of the basis function. The architecture of the fitting process allows for another useful measure of the quality of the fitting of the spectrum by comparing creatine 3.9 (Cr3.9) to creatine 3.0 (Cr3.0) ratios, which ideally should be 1 since the number of protons (2,3) are already taken into account for Cr3.9 and Cr3.0, respectively, in their basis-set creation. Higher Cr3.9/Cr3.0 ratios reflect poor spectra and implying that the results can be excluded. Note that in order to implement this control creatine 3.9 and creatine 3.0 have to be implemented as different elements in the basis sets. Our preliminary
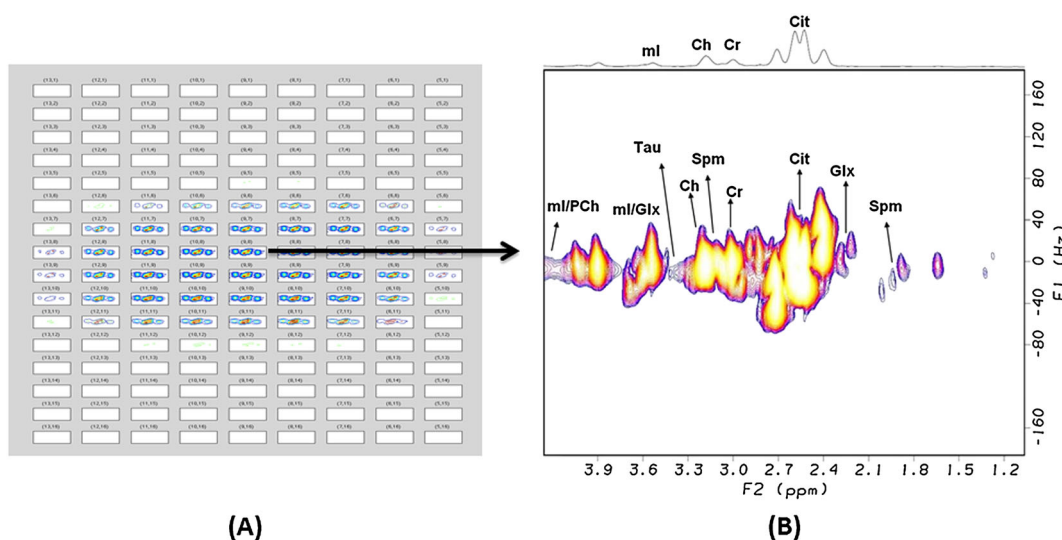

(A)   **(B)**

Figure 9. (A) The CS-reconstructed 2D J-resolved multivoxel spectra showing the Cit multiplets processed from the 25% NUS raw data using a 3 T MRI scanner. (B) the corresponding 2D J-resolved spectrum extracted from the center voxel.
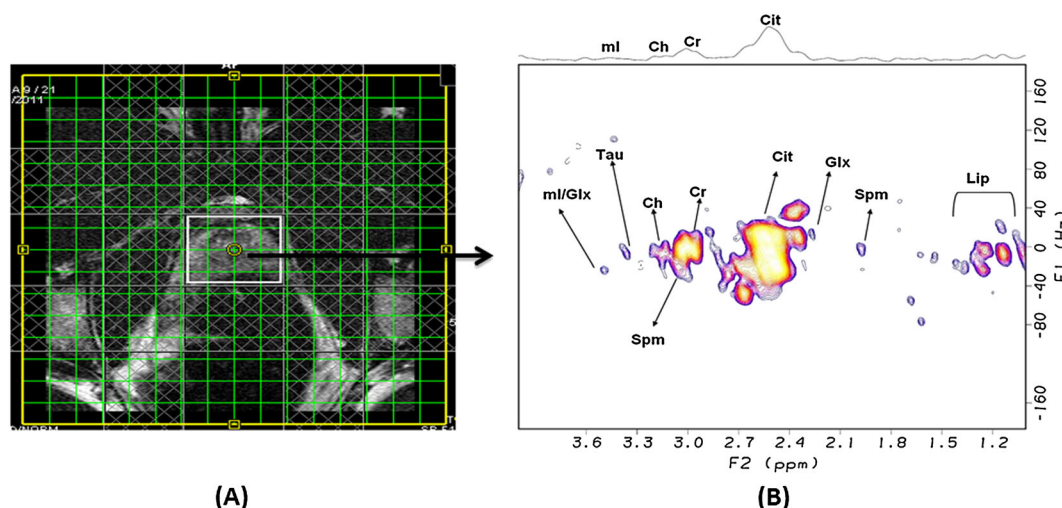
Figure 10. (A) An axial MRI slice of the 32 y.o. healthy male subject showing the VOI and MRSI grids. (B) The 2D J-resolved spectrum extracted from a 2 ml voxel. A 3 T MRI scanner was used.
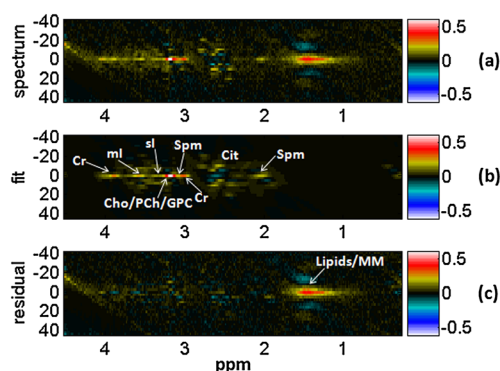

Figure 11. ProFit fitting of 2D JPRESS: (a) a 2D JPRESS spectrum recorded in the peripheral zone of the 27 y.o. healthy prostate using a 3 T MRI scanner, (b) its fit and (c) the fit residue as determined with ProFit.

results using the ProFit-based quantitation of the previously acquired GE 1.5 T and Siemens 3 T and 1.5 T MRS data using 2D localized-correlation spectroscopy (L-COSY) spectral acquisition in selected brain pathologies demonstrate the increased power of estimating more brain metabolites such as glutathione (GSH), PCh, PE, and GPC (109,110). Shown in Figure 11 are plots showing the fitting of a 2D JPRESS prostate spectrum (a) using a Siemens 3 T MRI scanner, the same as shown in Figure 5, its fit (b) and the fit residue (c) as determined with the ProFit algorithm. The estimated metabolite ratios (/Cr) using the ProFit quantitation were as follows: Cit, 7.36; PCh, 0.09; GPC, 0.48; Spm, 8.55; mI, 3.79; sI, 0.12; Glu, 1.52; Gln, 0.03; Tau, 1.47. These values were in agreement with the work published by Lange *et al.* (69). However, the applicability of ProFit in a clinical setting is yet to be demonstrated.

FUTURE DIRECTIONS: CLINICAL APPLICATIONS

As discussed above, localized 2D MRS has left infancy and moving to maturity. Twenty minutes of total duration were required for recording the decade old single-voxel-based 2D L-COSY and 2D JPRESS spectra. Recent fully sampled multivoxel-based 4D EP-JRESI and EP-COSI sequences enable recording 2D COSY and J-resolved

spectra in multiple regions. However, the total duration was typically 20–40 min depending on the number of incremented spectral (t_1) and spatial encoding (k_y) steps. Recent developments from our group demonstrate clearly that further acceleration can be accomplished using the NUS schemes and total durations of the 4D EP-JRESI and EP-COSI sequences can be shortened to approximately 10 min or less. The nonlinear CS reconstruction is necessary for processing the NUS 4D data. Further work is necessary to demonstrate the potential of multidimensional MR spectroscopic imaging using the fast imaging methods as reported recently to bring it into the clinic as a robust diagnostic metabolite imaging technique. We hope all these recent developments will lead to clinical realization of these novel MRSI sequences in the near future.

REFERENCES

1. Jemal A, Siegel R, Xu J, Ward E. Cancer statistics, 2010. CA Cancer J. Clin. 2010; 60(5): 277–300.
2. Gerber GS, Chodak GW. Routine screening for cancer of the prostate. J. Natl. Cancer Inst. 1991; 83(5): 329–335.
3. Gleason DF, Mellinger GT. Prediction of prognosis for prostatic adenocarcinoma by combined histological grading and clinical staging. J. Urol. 1974; 111(1): 58–64.
4. Amin M, Boccon-Gibod L, Egevad L, Epstein JI, Humphrey PA, Mikuz G, Newling D, Nilsson S, Sakr W, Srigley JR, Wheeler TM, Montironi R. Prognostic and predictive factors and reporting of prostate carcinoma in prostate needle biopsy specimens. Scand. J. Urol. Nephrol. 2005; 216: 20–33.
5. Carvalhal GF, Smith DS, Mager DE, Catalona WJ. Digital rectal examination for detecting prostate cancer at prostate specific antigen levels of 4 ng/mL or less. J. Urol. 1999; 161(3): 835–839.
6. Eastham JA, May R, Robertson JL, Sartor O, Kattan MW. Development of a nomogram that predicts the probability of a positive prostate biopsy in men with an abnormal digital rectal

examination and a prostate-specific antigen between 0 and 4 ng/mL. Urology 1999; 54(4): 708–713.

7. Catalona WJ, Richie JP, Ahmann FR, Hudson MA, Scardino PT, Flanigan RC, deKernion JB, Ratliff TL, Kavoussi LR, Dalkin BL, Waters WB, MacFarlane MT, Southwick PC. Comparison of digital rectal examination and serum prostate specific antigen (PSA) in the early detection of prostate cancer: results of a multicentre clinical trial of 6,630 men. J. Urol. 1994; 151(5): 1283–1290.

8. Schröder FH, van der Maas P, Beemsterboer P, Kruger AB, Hoedemaeker R, Rietbergen J, Kranse R. Evaluation of the digital rectal examination as a screening test for prostate cancer. Rotterdam section of the European Randomized Study of Screening for Prostate Cancer. J. Natl. Cancer Inst. 1998; 90(23): 1817–1823.

9. Schröder FH, Carter HB, Wolters T, van den Bergh RC, Gosselaar C, Bangma CH, Roobol MJ. Early detection of prostate cancer in 2007. Part 1: PSA and PSA kinetics. Eur. Urol. 2008; 53(3): 468–477.

10. Kurhanewicz J, Vigneron D, Carroll P, Coakley F. Multiparametric magnetic resonance imaging in prostate cancer: present and future. Curr. Opin. Urol. 2008; 18(1): 71–77.

11. Kurhanewicz J, Swanson MG, Nelson SJ, Vigneron DB. Combined magnetic resonance imaging and spectroscopic imaging approach to molecular imaging of prostate cancer. J. Magn. Reson. Imaging 2002; 16(4): 451–463.

12. Schiebler ML, Tomaszewski JE, Bezzi M, Pollack HM, Kressel HY, Cohen EK, Altman HG, Gefter WB, Wein AJ, Axel L. Prostatic carcinoma and benign prostatic hyperplasia: correlation of high-resolution MR and histopathologic findings. Radiology 1989; 172: 131–137.

13. Berman CG, Brodsky NJ. Prostate cancer imaging. Cancer Control 1998; 5: 541–554.

14. Beyersdorff D, Taupitz M, Winkelmann B, Fischer T, Lenk S, Loening SA, Hamm B. Patients with a history of elevated prostate-specific antigen levels and negative transrectal US-guided quadrant or sextant biopsy results: value of MR imaging. Radiology 2002; 224: 701–706.

15. Le Bihan D, Breton E, Lallemand D, Aubin ML, Vignaud J, Laval-Jeantet M. Separation of diffusion and perfusion in intravoxel incoherent motion MR imaging. Radiology 1988; 168: 497–505.

16. Miao H, Fukatsu H, Ishigaki T. Prostate cancer detection with 3-T MRI: comparison of diffusion-weighted and T2-weighted imaging. Eur. J. Radiol. 2007; 61: 297–302.

17. Lim HK, Kim JK, Kim KA, Cho KS. Prostate cancer: apparent diffusion coefficient map with T2-weighted images for detection – a multireader study. Radiology 2009; 250: 145–151.

18. Mazaheri Y, Hricak H, Fine SW, Akin O, Shukla-Dave A, Ishill NM, Moskowitz CS, Grater JE, Reuter VE, Zakian KL, Touijer KA, Koutcher JA. Prostate tumor volume measurement with combined T2-weighted imaging and diffusion weighted MR: correlation with pathologic tumor volume. Radiology 2009; 252: 449–457.

19. Carmeliet P, Jain RK. Angiogenesis in cancer and other diseases. Nature 2000; 407: 249–257.

20. Padhani AR, Husband JE. Dynamic contrast-enhanced MRI studies in oncology with an emphasis on quantification, validation and human studies. Clin. Radiol. 2001; 56: 607–620.

21. Bigler SA, Deering RE, Brawer MK. Comparison of microscopic vascularity in benign and malignant prostate tissue. Hum. Pathol. 1993; 24: 220–226.

22. Kiessling F, Lichy M, Grobholz R, Heilmann M, Farhan N, Michel MS, Trojan L, Ederle J, Abel U, Kauczor HU, Semmler W, Delorme S. Simple models improve the discrimination of prostate cancers from the peripheral gland by T1-weighted dynamic MRI. Eur. Radiol. 2004; 14: 1793–1801.

23. Mydlo JH, Kral JG, Volpe M, Axotis C, Macchia RJ, Pertschuk LP. An analysis of microvessel density, androgen receptor, p53 and HER-2/neu expression and Gleason score in prostate cancer: preliminary results and therapeutic implications. Eur. Urol. 1998; 34: 426–432.

24. Schlemmer HP, Merkle J, Grobholz R, Jaeger T, Michel MS, Werner A, Rabe J, van Kaick G. Can pre-operative contrast-enhanced dynamic MR imaging for prostate cancer predict microvessel density in prostatectomy specimens? Eur. Radiol. 2004; 14: 309–317.

25. Jager GJ, Ruijter ET, van de Kaa CA, de la Rosette JJ, Oosterhof GO, Thornbury JR, Ruijs SH, Barentsz JO. Dynamic TurboFLASH subtraction technique for contrast-enhanced MR imaging of the prostate: correlation with histopathologic results. Radiology 1997; 203: 645–652.

26. Preziosi P, Orlacchio A, Di Giambattista G, Di Renzi P, Bortolotti L, Fabiano A, Cruciani E, Pasqualetti P. Enhancement patterns of prostate cancer in dynamic MRI. Eur. Radiol. 2003; 13: 925–930.

27. Rouviere O, Raudrant A, Ecochard R, Colin-Pangaud C, Pasquiou C, Bouvier R, Maréchal JM, Lyonnet D. Characterization of time-enhancement curves of benign and malignant prostate tissue at dynamic MR imaging. Eur. Radiol. 2003; 13: 931–942.

28. Engelbrecht MR, Huisman HJ, Laheij RJ, Jager GJ, van Leenders GJ, Hulsbergen-Van De Kaa CA, de la Rosette JJ, Blickman JG, Barentsz JO. Discrimination of prostate cancer from normal peripheral zone and central gland tissue by using dynamic contrast-enhanced MR imaging. Radiology 2003; 229: 248–254.

29. McMahon CJ, Bloch BN, Lenkinski RE, Rofsky NM. Dynamic contrast-enhanced MR imaging in the evaluation of patients with prostate cancer. Magn. Reson. Imaging Clin. N. Am. 2009; 17: 363–383.

30. Bonekamp D, Macura KJ. Dynamic contrast-enhanced magnetic resonance imaging in the evaluation of the prostate. Top. Magn. Reson. Imaging 2008; 19: 273–284.

31. Macura KJ. Multiparametric magnetic resonance imaging of the prostate: current status in prostate cancer detection, localization, and staging. Semin. Roentgenol. 2008; 43: 303–313.

32. Futterer JJ, Heijmink SW, Scheenen TW, Veltman J, Huisman HJ, Vos P, Hulsbergen-Van de Kaa CA, Witjes JA, Krabbe PF, Heerschap A, Barentsz JO. Prostate cancer localization with dynamic contrast-enhanced MR imaging and proton MR spectroscopic imaging. Radiology 2006; 241: 449–458.

33. Ocak I, Bernardo M, Metzger G, Barrett T, Pinto P, Albert PS, Choyke PL. Dynamic contrast-enhanced MRI of prostate cancer at 3 T: a study of pharmacokinetic parameters. Am. J. Roentgenol. 2007; 189: 849.

34. Kim JK, Hong SS, Choi YJ, Park SH, Ahn H, Kim CS, Cho KS. Wash-in rate on the basis of dynamic contrast-enhanced MRI: usefulness for prostate cancer detection and localization. J. Magn. Reson. Imaging 2005; 22: 639–646.

35. Kim CK, Park BK, Kim B. Localization of prostate cancer using 3 T MRI – comparison of T2-weighted and dynamic contrast-enhanced imaging. J. Comput. Assist. Tomogr. 2006; 30: 7–11.

36. Engelbrecht MR, Huisman HJ, Laheij RJ, Jager GJ, van Leenders GJ, Hulsbergen-Van De Kaa CA, de la Rosette JJ, Blickman JG, Barentsz JO. Discrimination of prostate cancer from normal peripheral zone and central gland tissue by using dynamic contrast-enhanced MR imaging. Radiology 2003; 229: 248–254.

37. Ren J, Huan Y, Wang H, Chang YJ, Zhao HT, Ge YL, Liu Y, Yang Y. Dynamic contrast-enhanced MRI of benign prostatic hyperplasia and prostatic carcinoma: correlation with angiogenesis. Clin. Radiol. 2008; 63: 153–159.

38. Padhani AR, Gapinski CJ, Macvicar DA, Parker GJ, Suckling J, Revell PB, Leach MO, Dearnaley DP, Husband JE. Dynamic contrast enhanced MRI of prostate cancer: correlation with morphology and tumour stage, histological grade and PSA. Clin. Radiol. 2000; 55: 99–109.

39. Thomas MA, Narayan P, Kurhanewicz J, Jajodia P, Weiner MW. 1HMR spectroscopy of normal and malignant human prostates in vivo. J. Magn. Reson. 1990; 87: 610–619.

40. Kurhanewicz J, Vigneron DB, Nelson SJ, Hricak H, MacDonald JM, Konety B, Narayan P. Citrate as an in vivo marker to discriminate prostate cancer from benign prostatic hyperplasia and normal prostate peripheral zone: detection via localized proton spectroscopy. Urology 1995; 3: 459–466.

41. Govindaraju V, Young K, Maudsley AA. Proton NMR chemical shifts and coupling constants for brain metabolites. NMR Biomed. 2000; 13(3): 129–153.

42. Nagarajan R, Margolis D, Raman S, Sarma MK, Sheng K, King CR, Verma G, Sayre J, Reiter RE, Thomas MA. MR spectroscopic imaging and diffusion-weighted imaging of prostate cancer with Gleason scores. J. Magn. Reson. Imaging 2012; 36(3): 697–703.

43. Petroff OA, Rothman DL, Behar KL, Mattson RH. Initial observations on effect of vigabatrin on in vivo 1H spectroscopic measurements of gamma-aminobutyric acid, glutamate, and glutamine in human brain. Epilepsia 1995; 36(5): 457–464.

44. Trabesinger AH, Meier D, Boesiger P. In vivo 1H NMR spectroscopy of individual human brain metabolites at moderate field strengths. Magn. Reson. Imaging 2003; 21: 1295–1302.

45. Keltner JR, Wald LL, Christensen JD, Maas LC, Moore CM, Cohen BM, Renshaw PF. A technique for detecting GABA in the human brain with

PRESS localization and optimized refocusing spectral editing radiofrequency pulses. Magn. Reson. Med. 1996; 36: 458–461.

46. Rothman DI, Petroff OA, Behar KL, Mattson RH. Localized 1H NMR measurements of γ-aminobutyric acid in human brain in vivo. Proc. Natl Acad. Sci. USA 1993; 90: 5662–5666.

47. Lee HK, Yaman A, Nalcioglu O. Homonuclear J-refocused spectral editing technique for quantification of glutamine and glutamate by 1H NMR spectroscopy. Magn. Reson. Med. 1995; 34: 253–259.

48. Aue WP, Bartholdi E, Ernst RR. Two-dimensional spectroscopy – application to nuclear magnetic resonance. J. Chem. Phys. 1976; 64(5): 2229–2246.

49. Ryner LN, Sorenson JA, Thomas MA. 3-D localized 2D-NMR spectroscopy on an MRI scanner. J. Magn. Reson. B 1995; 107: 126–137.

50. Ryner LN, Sorenson JA, Thomas MA. Localized 2D J-resolved H-1 MR spectroscopy: strong coupling effects *in vitro and in vivo*. Magn. Reson. Imaging 1995; 13: 853–869.

51. Kreis R, Boesch C. Spatially localized, one- and two-dimensional NMR spectroscopy and in vivo application to human muscle. J. Magn. Reson. 1996; B113: 103–118.

52. Thomas MA, Yue K, Binesh N, Davanzo P, Kumar A, Siegel B, Frye M, Curran J, Lufkin R, Martin P, Guze B. Localized two dimensional shift correlated MR spectroscopy of human brain. Magn. Reson. Med. 2001; 46: 58–67.

53. Swanson MG, Vigneron DB, Tran TK, Sailasuta N, Hurd RE, Kurhanewicz J. Single-voxel oversampled J-resolved spectroscopy of in vivo human prostate tissue. Magn. Reson. Med. 2001; 45(6): 973–980.

54. Yue K, Marumoto A, Binesh N, Thomas MA. 2D JPRESS of human prostates using an endorectal receiver coil. Magn. Reson. Med. 2002; 47(6): 1059–1064.

55. Thomas MA, Binesh N, Yue K, Banakar S, Wyckoff N, Huda A, Marumoto A, Raman S. Adding a new spectral dimension to local-ized 1H MR spectroscopy of human prostates using an endorectal coil. Spectroscopy 2003; 17(2/3): 521–527.

56. Nagarajan R, Gomez AM, Raman SS, Margolis DJ, McClure T, Thomas MA. Correlation of endorectal 2D JPRESS findings with pathological Gleason scores in prostate cancer patients. NMR Biomed. 2010; 23 (3): 257–261.

57. Ernst RR, Bodenhausen G, Wokaun A. *Principles of NMR Spectroscopy in One and Two Dimensions*. Oxford University Press: Oxford; 1987, pp. 283–533.

58. Levitt MH. *Spin Dynamics: Basics of Nuclear Magnetic Resonance*. Wiley: Chichester, UK; 2002, pp. 361–383.

59. Keeler J. *Understanding NMR Spectroscopy*. Wiley: Cambridge; 2002.

60. Ziegler A, Izquierdo M, Remy C, Decorps M. Optimization of homonuclear two-dimensional correlation methods for in vivo and ex vivo NMR. J. Magn. Reson. 1995; B107: 10–18.

61. Kumar A. Two-dimensional spin-echo NMR spectroscopy: a general method for calculation of spectra. J. Magn. Reson. 1978; 30: 227–249.

62. Delikatny EJ, Hull WE, Mountford CE. The effect of altering time do-mains and window functions in two-dimensional proton COSY spectra of biological specimens. J. Magn. Reson. 1991; 94: 563–573.

63. Thrippleton MJ, Edden RAE, Keeler J. Suppression of strong coupling artefacts in J-spectra. J. Magn. Reson. 2005; 174: 97–109.

64. Smith SA, Levante TO, Meier BH, Ernst RR. Computer simulations in magnetic resonance. An object-oriented programming approach. J. Magn. Reson. 1994; 106A: 75–105.

65. Cheng LL, Wu C, Smith MR, Gonzalez RG. Non-destructive quantita-tion of spermine in human prostate tissue samples using HRMAS 1H NMR spectroscopy at 9.4 T. FEBS Lett. 2001; 494: 112–116.

66. Serkova NJ, Gamito EJ, Jones RH, O'Donnell C, Brown JL, Green S, Sullivan H, Hedlund T, Crawford ED. The metabolites citrate, myo-inositol, and spermine are potential age-independent markers of prostate cancer in human expressed prostatic secretions. Prostate 2008; 68: 620–628.

67. Van der Graaf M, Schipper RG, Oosterhof GO, Schalken JA, Verhofstad AA, Heerschap A. Proton MR spectroscopy of prostatic tissue focused on the detection of spermine, a possible biomarker of malignant behavior in prostate cancer. Magn. Reson. Mater. Phys. Biol. Med. 2000; 10: 153–159.

68. Mi Z, Kramer DL, Miller JT, Bergeron RJ, Bernacki R, Porter CW. Human prostatic carcinoma cell lines display altered regulation of polyamine transport in response to polyamine analogs and inhibi-tors. Prostate 1998; 34: 51–60.

69. Lange T, Schulte RF, Boesiger P. Quantitative J-resolved prostate spectroscopy using two-dimensional prior-knowledge fitting. Magn. Reson. Med. 2008; 59(5): 966–972.

70. Baker EH, Basso G, Barker PB, Smith MA, Bonekamp D, Horská A. Regional apparent metabolite concentrations in young adult brain measured by (1)H MR spectroscopy at 3 Tesla. J. Magn. Reson. Imaging 2008; 27(3): 489–499.

71. Mlynarik V, Gruber S, Moser E. Proton T(1) and T(2) relaxation times of human brain metabolites at 3 Tesla. NMR Biomed. 2001; 5: 325–331.

72. Schulte RF, Lange T, Beck J, Meier D, Boesiger P. Improved two-dimensional J-resolved spectroscopy. NMR Biomed. 2006; 19: 264–270.

73. Mansfield P. Spatial mapping of the chemical shift in NMR. Magn. Reson. Med. 1984; 1: 370–386.

74. Matsui S, Sekihara K, Kohno H. High speed spatially resolved NMR spectroscopy using phase modulated spin echo trains. Expansion of the spectral bandwidth by combined use of delayed spin echo trains. J. Magn. Reson. 1985; 64: 167–171.

75. Posse S, Tedeschi G, Risinger R, Ogg R, Bihan DL. High speed 1H spectroscopic imaging in human brain by echo planar spatial-spectral encoding. Magn. Reson. Med. 1995; 33: 34–40.

76. Ebel A, Soher BJ, Maudsley AA. Assessment of 3D proton MR echo-planar spectroscopic imaging using automated spectral analysis. Magn. Reson. Med. 2001; 46: 1072–1078.

77. Mulkern RV, Panych LP. Echo planar spectroscopic imaging. Concepts Magn. Reson. 2001; 13: 213–237.

78. Du W, Du YP, Fan X, Zamora MA, Karczmar GS. Reduction of spectral ghost artifacts in high-resolution echo-planar spectroscopic imag-ing of water and fat resonances. Magn. Reson. Med. 2003; 49(6): 1113–1120.

79. Chen AP, Cunningham CH, Ozturk-Isik E, Xu D, Hurd RE, Kelley DA, Pauly JM, Kurhanewicz J, Nelson SJ, Vigneron DB. High speed 3 T MR spectroscopic imaging of prostate with flyback echo-planar encoding. J. Magn. Reson. Imaging 2007; 25: 1288–1292.

80. Du W, Fan X, Foxley S, Zamora M, River JN, Culp RM, Karczmar GS. Comparison of high resolution echo-planar spectroscopic imaging with conventional MR imaging of prostate tumors in mice. NMR Biomed. 2005; 18: 285–292.

81. Lipnick S, Verma G, Ramadan S, Furuyama J, Thomas MA. Echo planar correlated spectroscopic imaging: implementation and pilot evalua-tion in human calf in vivo. Magn. Reson. Med. 2010; 64: 947–956.

82. Nagarajan R, Furuyama J, Margolis D, Raman S, Sarma M, Thomas M. Echo planar based J resolved and correlated spectroscopic imaging of human prostate using external coil. In: *Proceedings of the ISMRM, Montreal, Canada, 2011*. p. 2801.

83. Hennig J, Nauerth A, Friedburg H. RARE imaging: a fast imaging method for clinical MR. Magn. Reson. Med. 1986; 3: 823–833.

84. Constable R, Smith R, Gore J. Signal-to-noise and contrast in fast spin echo (FSE) and inversion recovery FSE imaging. J. Comput. Assist. Tomogr. 1992; 16(1): 41–47.

85. Listerud J, Einstein S, Outwater E, Kressel HY. First principles of fast spin echo. Magn. Reson. Q. 1992; 8(4): 199–244.

86. Duyn JH, Moonen CTW. Fast proton spectroscopic imaging of human brain using multiple spin-echoes. Magn. Reson. Med. 1993; 30: 409–414.

87. Dydak U, Meier D, Lamerichs R, Boesiger P. Trading spectral separa-tion at 3 T for acquisition speed in multi spin-echo spectroscopic imaging. Am. J. Neruroradiol. 2006; 27: 1441–1446.

88. Rutgers DR, van der Grond J. Relaxation times of choline, creatine and N-acetyl aspartate in human cerebral white matter at 1.5 T. NMR Biomed. 2002; 3: 215–221.

89. Nagarajan R, Furuyama J, Sarma MK, Margolis D, Raman S, Reiter RE. Multi-echo EP-based J-resolved magnetic resonance spectroscopic imaging of prostate cancer. In: *RSNA–Scientific Meeting 2011 (Chicago, USA)*. Abstract 186.

90. Donoho D. Compressed sensing. IEEE Trans. Info. Theory 2006; 52: 1289–1306.

91. Candez EJ, Romberg J, Tao T. Stable signal recovery from incom-plete and inaccurate measurements. Commun. Pure Appl. Math. 2006; 59: 1207–1221.

92. Lustig M, Donoho D, Pauly JM. Sparse MRI: the application of com-pressed sensing for rapid MR imaging. Magn. Reson. Med. 2007; 58 (6): 1182–1195.

93. Doneva M, Börnert P, Eggers H, Mertins A, Pauly J, Lustig M. Compressed sensing for chemical shift-based water–fat separation. Magn. Reson. Med. 2010; 64(6): 1749–1759.

94. Hu S, Lustig M, Chen AP, Crane J, Kerr A, Kelley DA, Hurd R, Kurhanewicz J, Nelson SJ, Pauly JM, Vigneron DB. Compressed sensing for resolution enhancement of hyperpolarized 13C flyback 3D-MRSI. J. Magn. Reson. 2008; 192(2): 258–264.

95. Gamper U, Boesiger P, Kozerke S. Compressed sensing in dynamic MRI. Magn. Reson. Med. 2008; 59: 365–373.

96. Michailovich O, Rathi Y, Dolui S. Spatially regularized compressed sensing for high angular resolution diffusion imaging. IEEE Trans. Med. Imaging 2011; 30: 1100–1115.

97. Wu B, Millane RP, Watts R, Bones PJ. Prior estimate based compressed sensing in parallel MRI. Magn. Reson. Med. 2011; 65: 83–95.

98. Hu S, Lustig M, Balakrishnan A, Larson PE, Bok R, Kurhanewicz J, Nelson SJ, Goga A, Pauly JM, Vigneron DB. 3D compressed sensing for highly accelerated hyperpolarized 13C MRSI with in vivo applications to transgenic mouse models of cancer. Magn. Reson. Med. 2010; 63: 312–321.

99. Scheenen TW, Heijmink SW, Roell SA, Hulsbergen-Van de Kaa CA, Knipscheer BC, Witjes JA, Barentsz JO, Heerschap A. Three-dimensional proton MR spectroscopy of human prostate at 3 T without endorectal coil: feasibility. Radiology 2007; 245: 507–516.

100. Kim DH, Margolis D, Xing L, Daniel B, Spielman D. In vivo prostate magnetic resonance spectroscopic imaging using two-dimensional J-resolved PRESS at 3 T. Magn. Reson. Med. 2005; 53(5): 1177–1182.

101. Goldstein T, Osher S. The split Bregman method for L1-regularized problems. SIAM Journal on Imaging Sciences 2009; 2(2): 323–343.

102. Furuyama J, Wilson N, Burns B, Nagarajan R, Margolis D, Thomas MA. Application of compressed sensing to multidimensional spectroscopic imaging in human prostate. Magn. Reson. Med. 2012; 67: 1499–1505.

103. DeFeo EM, Cheng LL. Characterizing human cancer metabolomics with *ex vivo* 1H HRMAS MRS. Technol. Cancer Res. Treat. 2010; 9: 381–391.

104. Stenman K, Stattin P, Stenlund H, Riklund K, Gröbner G, Bergh A. 1H HRMAS NMR derived biomarkers related tumor grade, tumor cell fraction, and cell proliferation in prostate tissue samples. Biomarker Insights 2011; 6: 39–47.

105. Swanson MG, Vigneron DB, Tabatabai ZL, Males RG, Schmitt L, Carroll PR, James JK, Hurd RE, Kurhanewicz J. Proton HR-MAS spectroscopy and quantitative pathologic analysis of MRI/3D-MRSI-targeted post-surgical prostate tissues. Magn. Reson. Med. 2003; 50: 944–954.

106. Wright A, Tessem MB, Bertilsson H, Grinde MT, Giskeødegård GF, Halgunset J, Angelsen A, Heerschap A, Gribbestad IS. Quantitative 1H MR Model shows glutamate, choline, glycerylphosphocholine, and glucose as biomarkers of prostate. Proc. Intl Soc. Magn. Reson. Med. 2012; 20: 2975.

107. Thomas MA, Lange T, Velan SS, Nagarajan R, Raman S, Gomez A, Margolis D, Swart S, Raylman RR, Schulte RF, Boesiger P. Two-dimensional MR spectroscopy of healthy and cancerous prostates in vivo. Magn. Reson. Mater. Phys. Biol. Med. 2008; 21(6): 443–458.

108. Cavassila S, Deval S, Huegen C, van Ormondt D, Graveron-Demilly D. Cramer–Rao bound expressions for parametric estimation of overlapping peaks: influence of prior knowledge. J. Magn. Reson. 2000; 143(2): 311–320.

109. Sarma MK, Huda A, Nagarajan R, Hinkin CH, Wilson N, Gupta RK, Frias-Martinez E, Sayre J, Guze B, Han SH, Thomas MA. Multi-dimensional MR spectroscopy: towards a better understanding of hepatic encephalopathy. Metab. Brain Dis. 2011; 26(3): 173–184.

110. Nagarajan R, Sarma MK, Thames AD, Castellon SA, Hinkin CH, Thomas MA. 2D MR spectroscopy combined with prior-knowledge fitting is sensitive to HCV associated cerebral metabolic abnormalities. Int. J. Hepatol. 2012; 2012: 179365.